BAMS Article

The Ny-Ålesund Aerosol Cloud Experiment (NASCENT)

Overview and First Results

J. T. Pasquier, R. O. David, G. Freitas, R. Gierens, Y. Gramlich, S. Haslett, G. Li, B. Schäfer, K. Siegel, J. Wieder, K. Adachi, F. Belosi, T. Carlsen, S. Decesari, K. Ebell, S. Gilardoni, M. Gysel-Beer, J. Henneberger, J. Inoue, Z. A. Kanji, M. Koike, Y. Kondo, R. Krejci, U. Lohmann, M. Maturilli, M. Mazzolla, R. Modini, C. Mohr, G. Motos, A. Nenes, A. Nicosia, S. Ohata, M. Paglione, S. Park, R. E. Pileci, F. Ramelli, M. Rinaldi, C. Ritter, K. Sato, T. Storelvmo, Y. Tobo, R. Traversi, A. Viola, and P. Zieger

ABSTRACT: The Arctic is warming at more than twice the rate of the global average. This warming is influenced by clouds, which modulate the solar and terrestrial radiative fluxes and, thus, determine the surface energy budget. However, the interactions among clouds, aerosols, and radiative fluxes in the Arctic are still poorly understood. To address these uncertainties, the Ny-Ålesund Aerosol Cloud Experiment (NASCENT) study was conducted from September 2019 to August 2020 in Ny-Ålesund, Svalbard. The campaign's primary goal was to elucidate the life cycle of aerosols in the Arctic and to determine how they modulate cloud properties throughout the year. In situ and remote sensing observations were taken on the ground at sea level, at a mountaintop station, and with a tethered balloon system. An overview of the meteorological and the main aerosol seasonality encountered during the NASCENT year is introduced, followed by a presentation of first scientific highlights. In particular, we present new findings on aerosol physicochemical and molecular properties. Further, the role of cloud droplet activation and ice crystal nucleation in the formation and persistence of mixed-phase clouds, and the occurrence of secondary ice processes, are discussed and compared to the representation of cloud processes within the regional Weather Research and Forecasting Model. The paper concludes with research questions that are to be addressed in upcoming NASCENT publications.

KEYWORDS: Atmosphere; Arctic; Cloud microphysics; Cloud radiative effects; Aerosols; Aerosol-cloud interaction

https://doi.org/10.1175/BAMS-D-21-0034.1
Corresponding authors: Julie T. Pasquier, julie.pasquier@env.ethz.ch; Paul Zieger, paul.zieger@aces.su.se
Supplemental material: https://doi.org/10.1175/BAMS-D-21-0034.2

In final form 8 June 2022

AFFILIATIONS: Pasquier, Li, Wieder, Henneberger, Kanji, Lohmann, and Ramelli—Institute for Atmospheric and Climate Science, ETH Zürich, Zurich, Switzerland; **David, Schäfer, Carlsen, and Storelvmo**—Department of Geosciences, University of Oslo, Oslo, Norway; **Freitas, Gramlich, Haslett, Siegel, Krejci, Mohr, and Zieger**—Department of Environmental Science, and Bolin Centre for Climate Research, Stockholm University, Stockholm, Sweden; **Gierens and Ebell**—Institute for Geophysics and Meteorology, University of Cologne, Cologne, Germany; **Adachi**—Meteorological Research Institute, Tsukuba, Ibaraki, Japan; **Belosi, Decesari, Nicosia, Paglione, and Rinaldi**—National Research Council, Institute of Atmospheric Sciences and Climate (CNR-ISAC), Bologna, Italy; **Gilardoni, Mazzolla, and Viola**—Institute for Polar Sciences, CNR, Bologna, and Institute for Polar Sciences, CNR, Rome, Italy; **Gysel-Beer and Modini**—Laboratory of Atmospheric Chemistry, Paul Scherrer Institute, Villigen, Switzerland; **Inoue, Kondo, and Tobo**—National Institute of Polar Research, Tachikawa, Tokyo, Japan; **Koike**—Department of Earth and Planetary Science, Graduate School of Science, The University of Tokyo, Tokyo, Japan; **Maturilli and Ritter**—Alfred Wegener Institute, Helmholtz Centre for Polar and Marine Research, Potsdam, Germany; **Motos**—Laboratory of Atmospheric Processes and Their Impacts, Ecole Polytechnique Fédérale de Lausanne, Lausanne, Switzerland; **Nenes**—Laboratory of Atmospheric Processes and Their Impacts, Ecole Polytechnique Fédérale de Lausanne, Lausanne, Switzerland, and Center for Studies of Air Quality and Climate Change, Institute for Chemical Engineering Sciences, Foundation for Research and Technology Hellas, Patras, Greece; **Ohata**—Institute for Space–Earth Environmental Research, and Institute for Advanced Research, Nagoya University, Nagoya, Aichi, Japan; **Park**—Korea Polar Research Institute, Incheon, Korea; **Pileci**—Laboratory of Atmospheric Chemistry, Paul Scherrer Institute, Villigen, Switzerland, and U-Earth Biotech Ltd., London, United Kingdom; **Sato**—Kitami Institute of Technology, Kitami, Hokkaido, Japan; **Traversi**—Department of Chemistry, University of Florence, Florence, Italy

Average temperatures over the Arctic region have increased by a factor of 2–3 compared to the global average rate in the past few decades (e.g., Wendisch et al. 2017). This phenomenon is known as Arctic amplification (AA) and causes the retreat of sea ice at the alarming rates currently observed (e.g., Bennartz et al. 2013; Cohen et al. 2014). Several feedback mechanisms contribute to AA, but their relative importance in different regions of the Arctic is still under discussion (e.g., Hall et al. 2021). The sea ice albedo feedback is often proposed as the main driver of AA (e.g., Deser et al. 2000). However, model experiments have shown that AA occurs even in the absence of sea ice and snow cover changes (e.g., Graversen and Wang 2009). Despite their potentially large impact on the AA, the feedback processes related to aerosols and clouds are especially poorly understood (e.g., Morrison et al. 2012; Pithan and Mauritsen 2014; Wendisch et al. 2017; Goosse et al. 2018).

The role of aerosols in the Arctic climate is especially complex due to the diverse processes that control their abundance and their chemical and physical properties (e.g., Willis et al. 2018). Knowledge gaps in aerosol sources, sinks, and transformation processes, and uncertainties in aerosol–cloud interactions are among the reasons why current climate models have difficulties reproducing the current and future climate in the Arctic (Schmale et al. 2021). At Ny-Ålesund on Svalbard, the potential aerosol particle sources and sinks show a strong seasonality (Tunved et al. 2013; Ström et al. 2003). Primary particles can originate from natural sources such as oceans (e.g., sea spray, primary biological particles) or glaciers (e.g., soil dust) (Weinbruch et al. 2012; Tobo et al. 2019; Heslin-Rees et al. 2020). Particles from forest fires or anthropogenic emissions can be transported from lower latitudes to Svalbard (Stohl et al. 2007; Schacht et al. 2019). Secondary particles can be formed locally from

gas-to-particle conversion processes involving anthropogenic and natural precursor gases (e.g., Dall'Osto et al. 2017; Nielsen et al. 2019; Beck et al. 2020; H. Lee et al. 2020; Brean et al. 2021; Choi et al. 2019). However, quantitative knowledge about the physicochemical properties of Arctic aerosols and precursor gases remains limited, especially during the Arctic winter, which renders an accurate source apportionment and the estimation of their impact difficult.

Clouds influence downwelling solar and terrestrial radiative fluxes that determine the surface energy budget (e.g., Curry et al. 1996; Shupe and Intrieri 2004). On the one hand, clouds scatter solar radiation back to space, leading to a shortwave cooling effect at the surface. On the other hand, they emit longwave radiation to space and back to the surface and, therefore, have a longwave warming effect at the surface (Lohmann et al. 2016; Nomokonova et al. 2019; Ebell et al. 2020). The impact clouds have on the energy budget depends on their macro- and microphysical properties (e.g., Shupe and Intrieri 2004; Dong et al. 2010; Sedlar et al. 2012). The optical thickness of a pure ice cloud is lower for a given cloud water path because ice particles are fewer and larger than corresponding liquid droplets and have a different refractive index, i.e., ice clouds have lower albedos and longwave emissivities (Sun and Shine 1994; Korolev 2007). Arctic mixed-phase clouds (MPCs), consisting of cloud droplets and ice crystals, particularly influence the Arctic surface radiation balance (e.g., Curry et al. 1996; Shupe and Intrieri 2004; Goosse et al. 2018). Their albedos and emissivities lie between the ones of pure ice and pure liquid clouds, and depend on the exact mixture of the phases (Sun and Shine 1994) which is strongly influenced by aerosols. Aerosols acting as cloud condensation nuclei (CCN) are required to form cloud droplets and aerosols termed ice-nucleating particles (INPs) are needed to form primary ice crystals. Once primary ice crystals are formed, secondary ice production (SIP) can occur (e.g., Hallett and Mossop 1974; Takahashi et al. 1995; Korolev et al. 2020; Korolev and Leisner 2020) and enhance the ice crystal number concentration (ICNC) by several order of magnitudes (Korolev et al. 2020). Consequently, aerosol particles acting as CCN and INPs as well as SIP determine the phase partitioning within MPCs, which ultimately influences the radiation budget.

The phase partitioning within MPC impacts the lifetime of Arctic MPCs. The mixture of ice crystals and cloud droplets is thermodynamically unstable and the so-called Wegener–Bergeron–Findeisen (WBF) process (Wegener 1911; Bergeron 1935; Findeisen 1938) can cause a complete glaciation of the cloud within a few hours (Harrington et al. 1999; Rangno and Hobbs 2001; Korolev and Isaac 2003). However, Arctic MPCs are surprisingly persistent over several hours or days (e.g., Zuidema et al. 2005; Morrison et al. 2012). The current understanding obtained from modeling and theoretical studies is that self-maintaining feedbacks between liquid water, radiation, and turbulent updrafts are responsible for the persistence of Arctic MPCs (Morrison et al. 2012). Although a number of studies have focused on the microphysical properties of Arctic MPCs (e.g., McFarquhar et al. 2011; Lloyd et al. 2015; Young et al. 2016; Wendisch et al. 2019), the processes controlling the life cycle of Arctic MPCs still remain poorly understood (e.g., Tjernström et al. 2014; Mioche et al. 2015).

The Ny-Ålesund Aerosol Cloud Experiment (NASCENT) campaign was conducted to enhance our knowledge on Arctic aerosols and clouds, and their complex interactions throughout the polar year. The former mining town of Ny-Ålesund, located on the western part of the Norwegian archipelago of Svalbard (Fig. 1), is nowadays fully dedicated to research. Ny-Ålesund is a unique place to study aerosol–cloud interactions and their potential influence on climate as the Svalbard region is frequently covered by MPCs susceptible to aerosol perturbations (Mioche et al. 2015) and experiences the largest warming within the Arctic (Dahlke and Maturilli 2017; Susskind et al. 2019). The NASCENT study was designed to obtain a comprehensive set of cloud and aerosol observations to address in particular the following questions:

- What are the factors that determine the ability of aerosol particles to act as CCN and INPs in the Arctic?
- What are the sources, precursor gases, chemical composition, molecular properties, and the seasonality of these cloud forming aerosols?
- Under which conditions do INPs or SIP dominantly influence the phase partitioning in Arctic MPCs?

The general setup and main instrumentation of NASCENT are introduced in the second section. All acronyms used throughout the manuscript are summarized in Table 1. An overview of the temperature, wind, aerosol, and cloud seasonality during NASCENT is given in the third section. In the fourth section, first research highlights on aerosol and cloud interactions are discussed. Finally, a summary is given in the fifth section, including questions to be answered in the forthcoming data analyses of the NASCENT study.

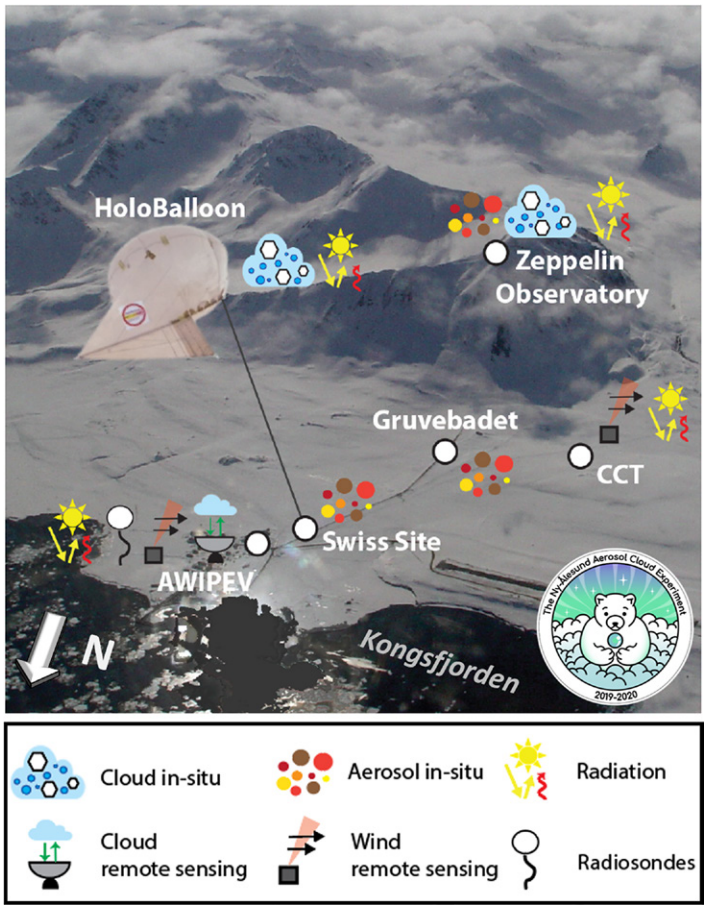

Fig. 1. Overview of the NASCENT study setup at Ny-Ålesund, Svalbard. Aerial photo with the five measurement locations and the respective instrumentation. The campaign logo is shown in the lower-right corner. Note that a topographic map with terrain contours is shown in Fig. 4.

NASCENT study design

Measurement site. The NASCENT study took place at Ny-Ålesund (78.9°N, 11.9°E), located on the west coast of Svalbard, from September 2019 through August 2020. Ny-Ålesund is situated on the south side of Kongsfjorden and surrounded by glaciers, moraines, rivers, mountains, and a typical tundra ecosystem. During NASCENT, atmospheric measurements were performed at five locations close to Ny-Ålesund (Fig. 1). The atmospheric observatory of the AWIPEV research base and the Swiss site are located at the southwestern edge of town. The Zeppelin Observatory is located 2 km southwest of Ny-Ålesund at 475 m MSL. Further measurements were performed at the Gruvebadet laboratory located about 1 km southward and at the Amundsen-Nobile Climate Change Tower (CCT) 1 km southwestward of the town.

Experimental setup. Aerosol, cloud, radiation, and meteorological properties were characterized using a multifaceted suite of instrumentation ranging from in situ to remote sensing techniques. An overview of the retrieved parameters at the different locations is given in Fig. 1 and in Table 2. Further details of the setup and a table with the data coverage are provided in the online supplementary information (SI; https://doi.org/10.1175/BAMS-D-21-0034.2).

At the Zeppelin Observatory [see, e.g., Platt et al. (2022) for a review of the last 30 years of observations], detailed in situ aerosol and cloud observations and meteorological parameters were taken using a multitude of complementary instrument techniques. At the temporary Swiss

Table 1. List of abbreviations and acronyms.

AA	Arctic amplification
BC	Black carbon
APS	Aerodynamic Particle Sizer
CCN	Cloud condensation nuclei
CCT	Climate Change Tower
CCNC	Cloud condensation nuclei counter
CDNC	Cloud droplet number concentration
CDP2	Cloud Droplet Probe
COSMOS	Continuous soot monitoring system
CPC	Condensation particle counter
CRAFT	Cryogenic Refrigerator Applied to Freezing Test
CVI	Counterflow virtual impactor
CPNC	Cloud particle number concentration
DFPC	Dynamic Filter Processing Chamber
DMA	Dimethylamine
DMPS	Differential Mobility Particle Sizer
DRINCZ	Droplet Ice Nuclei Counter Zurich
eBC	Equivalent black carbon
FIDAS	Fine Dust Measurement Device
FIGAERO-CIMS	Iodide chemical ionization high-resolution time-of-flight mass spectrometer coupled to a Filter Inlet for Gases and Aerosols coupled to a chemical ionization mass spectrometer
Gly	Glycerol
H-NMR	Proton-nuclear magnetic resonance spectroscopy
HMSA	Hydroxymethane-sulfonic acid
HINC	Horizontal Ice Nucleating Chamber
HOLIMO	Holographic Imager for Microscopic Objects
ICNC	Ice Crystal Number Concentration
INP	Ice nucleating particle
INPC	Ice nucleating particles concentration
IWC	Ice water content
L	Levoglucosan
LDNC	Liquid droplet number concentration
LWC	Liquid water content
LWP	Liquid water path
MAAP	Multiangle absorption photometer
MBS	Multiparameter Bioaerosol Spectrometer
MPC	Mixed-phase clouds
MSA	Methane-sulfonic acid
NASCENT	Ny-Ålesund Aerosol Cloud Experiment
OPC	Optical particle counter
p	Pressure
PAMTRA	The Passive and Active Microwave radiative Transfer tool
PM1	Particulate matter smaller than 1 μm
PM10	Particulate matter smaller than 10 μm
PSAP	Particle Soot Absorption Photometer
rBC	Refractory black carbon
RH	Relative humidity
SIP	Secondary ice production
SI	Supplementary information
SMPS	Scanning Mobility Particle Sizer
SP2-XR	Extended-range single-particle soot photometer
T	Temperature
TMA	Trimethylamine
WBF	Wegener–Bergeron–Findeisen process
WIBS	Wideband Integrated Bioaerosol Sensor
WRF	Weather Research and Forecasting Model

Table 2. Retrieved variables at the five measurement locations. The black crosses show long-term measurements and the measurements performed only during NASCENT are represented with the symbol "N." Parameters that were in addition measured behind the ground-based counterflow virtual impactor (CVI) inlet are marked by an asterisk (*).

	Measured quantities	Zeppelin obs.	HoloBalloon	Swiss site	Gruvebadet	CCT	AWIPEV
Meteorology	Wind vector	X	N	N		X	X
	Temperature	X	N	N	X	X	X
	RH	X		N	X	X	X
	Precipitation		N	N	X	X	X
	Vertical profiles of *T*, *p*, RH						X
	Vertical profiles wind vector					X	X
Cloud	Phase-resolved particle number size distribution	N	N				
	IWC	N	N				X
	LWC or LWP	N	N				X
	Ice crystal habits	N	N				
	Base and top height		N				X
	Radar reflectivity factor						X
Aerosol	Particle size distribution	X*		N	X		
	CCN properties	X*		N			
	INP concentration	X		N	X		
	Chemical composition	X/N*			N		
	Total particle concentration	X*			N		
	Particle size, shape, fluorescence	N*		N			
	Black carbon	X/N*			X		
	Single-particle analysis	X*					
Radiation	Broadband shortwave and longwave	X	N			X	X

site, ambient aerosol, CCN, and INP concentrations (INPC) were sampled through a heated inlet mounted on top of the measurement container. The holographic imager HOLIMO3B was mounted on the tethered balloon system HoloBalloon (Ramelli et al. 2020) to obtain in situ phase-resolved particle size distributions up to an altitude of 1000 m MSL. At the AWIPEV Observatory, long-term measurements are conducted to monitor the Arctic atmosphere including a cloud radar, a ceilometer, and a wind lidar. During intensive observation periods, additional radiosondes were launched to supplement the standard daily launches. Furthermore, meteorological parameters (e.g., temperature, humidity, wind speed and direction) and surface-based radiation fluxes were monitored (Maturilli et al. 2013a; Maturilli 2020). At Gruvebadet, aerosol properties (e.g., Becagli et al. 2019; Turetta et al. 2021), black carbon (BC) concentration, INPC, and chemical characterization of organic aerosol (PM1) were monitored. Furthermore, wind speed and direction, temperature, and radiation were measured on the 33-m-high CCT. Note that because of the distance between the five measurement locations, there are small spatial (up to 2 km) and temporal (up to a few minutes) differences between the measurements at the different sites. The combination of these measurements provides the opportunity to investigate aerosol–cloud interactions in the Arctic at an unprecedented scale. To exemplify the use of this multifaceted dataset, we use the Advanced Weather Research and Forecasting (WRF) Model, version 4.2.1 (Skamarock et al. 2019), to evaluate the model representation of an MPC when prescribing the measured CCN and INP concentrations.

Seasonality of meteorological, aerosol, and cloud parameters during NASCENT

Temperature. During NASCENT, unusually cold temperatures during the winter and spring (up to 6°C colder) were experienced (Fig. 2a). The anomalously cold temperatures during

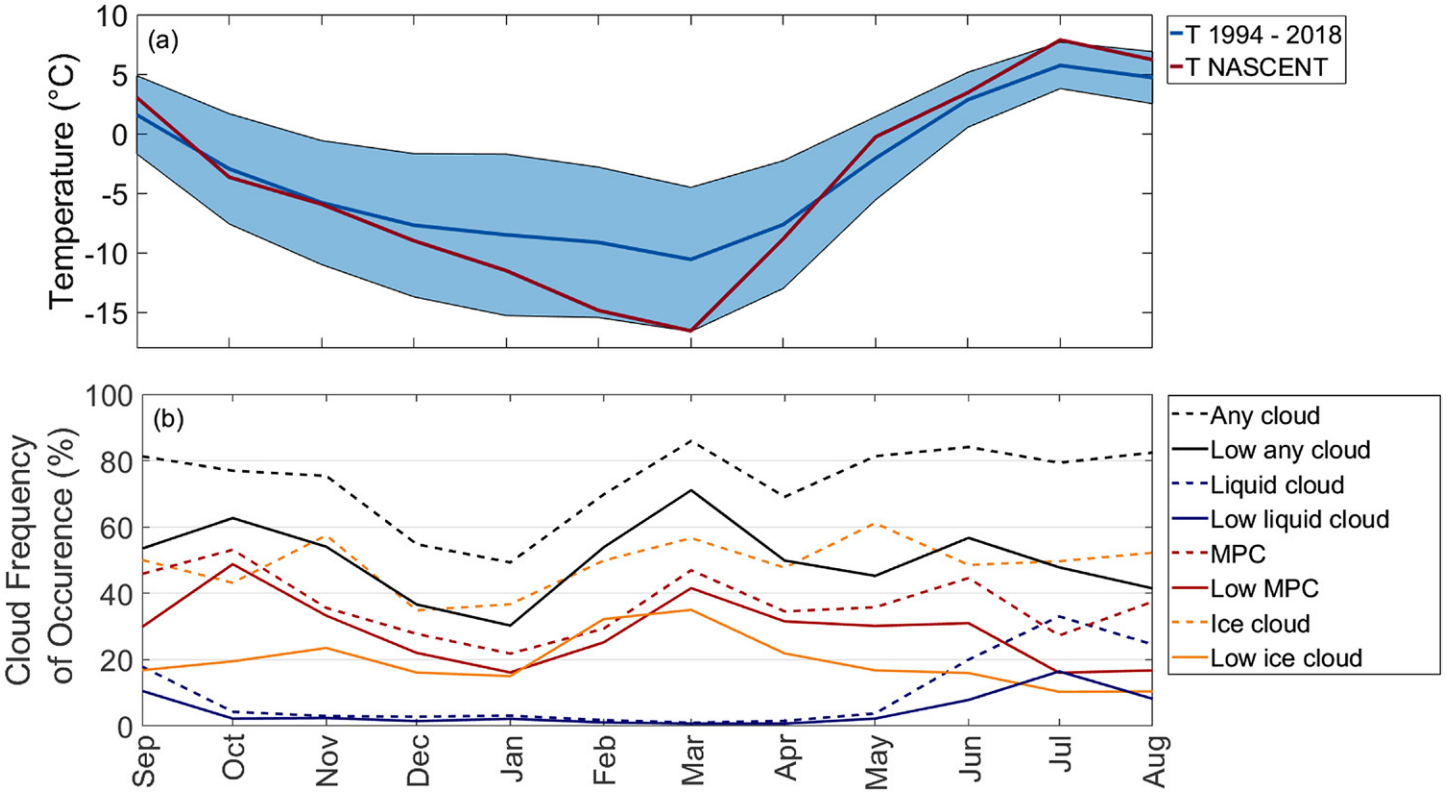

Fig. 2. Temperature and cloud seasonality observed during NASCENT. (a) Average temperatures during NASCENT compared to the climatology of 1994–2018 (shading represents the standard deviation) measured at the AWIPEV weather mast 10 m above ground (Maturilli et al. 2013b). (b) Monthly frequency of occurrence of cloud types derived from the Cloudnet data during NASCENT. Colors represent the different cloud types, while dashed lines show all clouds in the column and solid lines the low-level clouds with cloud tops below 3 km. Note that multiple cloud layers of different kinds are accounted for separately, so that the sum of "liquid," "ice," and "mixed phase" does not equal the frequency of "any" clouds.

February and March can be attributed to the exceptionally strong and cold stratospheric polar vortex (Lawrence et al. 2020; S. H. Lee et al. 2020). The low temperatures caused the rare freezing of the Kongsfjorden from February to April 2020, which likely limited the emission of local biological aerosols from the fjord. Although this may have led to a lower abundance of aerosol particles, no significant deviation from previous observations was observed (Fig. 3a). During the summer months, above normal temperatures were observed (up to 2°C, Fig. 2a) but with little to no detectable changes in the cloud and aerosol climatologies (Figs. 2b and 3).

Wind. The wind at Ny-Ålesund is strongly influenced by the surrounding topography, especially by the mountains, Kongsfjorden, and the glaciers. The wind measured 10 m above ground on the measurement field of the AWIPEV Observatory predominantly came from the southeast and less frequently from the southwest and northwest (Fig. 4). The wind speed was generally moderate (below 9 m s^{-1}). These results are in agreement with previous studies showing that the wind is channeled along the Kongsfjorden (Beine et al. 2001; Maturilli et al. 2013a; Maturilli and Kayser 2017). The effect of topography can be seen when comparing the wind measurements at AWIPEV to the ones taken at the CCT where the main wind direction was also from the southeast but had more frequent periods of southwesterly winds (Fig. 4), which is related to the katabatic outflow from the Brøggerbreen glaciers channeled along the slopes of the Zeppelin Mountain Range (Maturilli et al. 2013a). As the surface airflow is determined by the topography, local aerosol sources are likely to dominate over large-scale transport of aerosol under stable atmospheric conditions at the lower-altitude locations around Ny-Ålesund.

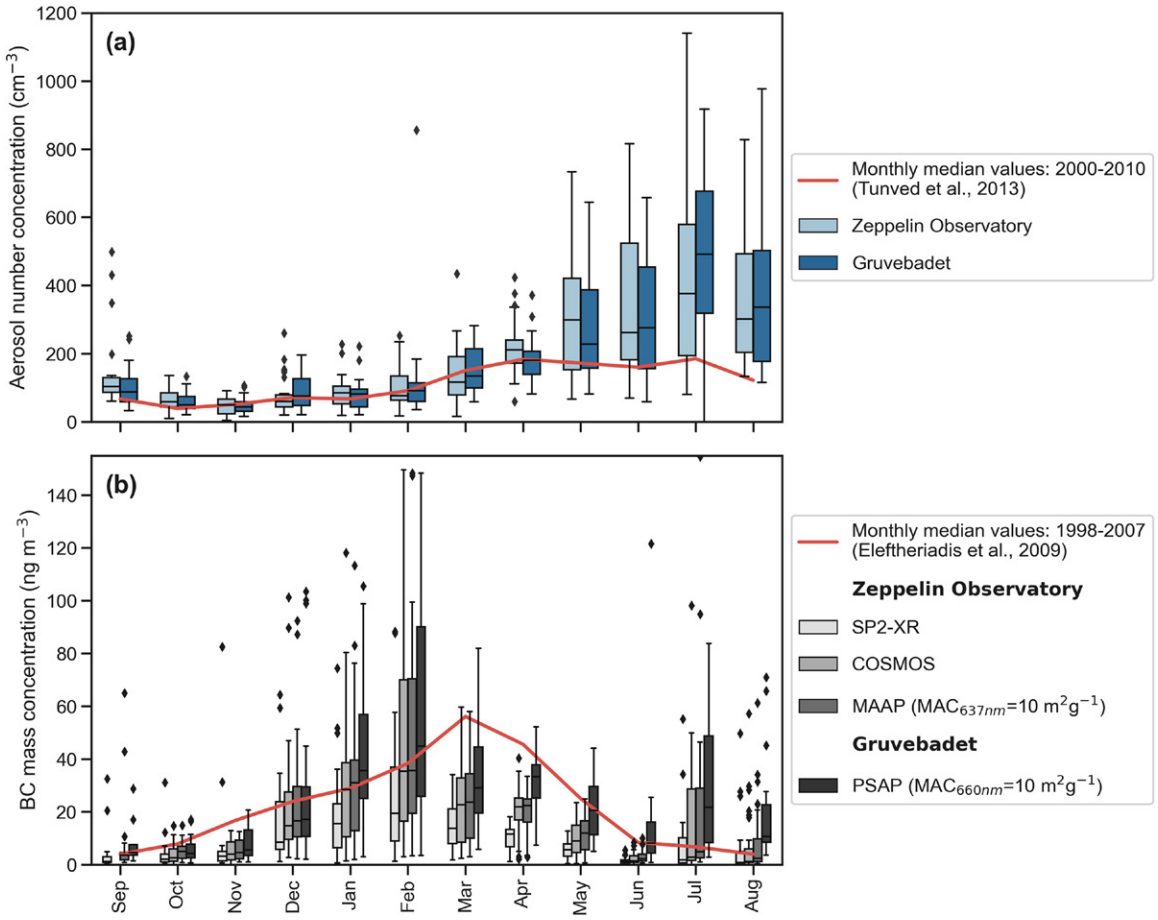

Fig. 3. Monthly average distributions of (a) aerosol particle number and (b) black carbon (BC) mass concentrations measured during NASCENT at Gruvebadet and at the Zeppelin Observatory in comparison to previous climatologies. The box-and-whisker plots show the quartiles and the 5th and 95th percentiles, respectively, while outliers are marked with diamonds. The particle number concentrations were measured using CPCs, while BC concentrations were measured by four different instruments: extended-range single-particle soot photometer (SP2-XR; Stephens et al. 2003; Schwarz et al. 2006), a multiangle absorption photometer (MAAP; Petzold and Schönlinner 2004), a continuous soot monitoring system (COSMOS; Kondo et al. 2011), and a Particle Soot Absorption Photometer (PSAP).

At the Zeppelin Observatory, the prevailing wind showed more southerly components with occasional periods of north to northwesterly wind (Fig. 4), which is in agreement with previous studies (Beine et al. 2001). This dominant wind component is due to the channeling between Zeppelin Mountain on the southwest side and a smaller hill on the east side of the observatory. This mountain blocks the large-scale winds and are responsible for the relatively low wind speed at the observatory (mostly below 6 m s^{-1}). Nevertheless, the air at Zeppelin Observatory is often above the local inversion and, therefore, less influenced by local aerosol sources compared to the other sites around Ny-Ålesund (e.g., Platt et al. 2022) as shown below.

Consistent with the surface winds being influenced by the terrain surrounding Ny-Ålesund, the radiosonde measurements between 3,000 m and 3,500 m MSL show that southwesterly to northwesterly winds were most frequently observed above Ny-Ålesund (Fig. 4), in agreement with the climatological wind observed by Maturilli and Kayser (2017).

Aerosols. Aerosol particles at Ny-Ålesund follow a typical seasonal cycle that is governed by the seasonality of the particles' respective sources and sinks (e.g., Tunved et al. 2013; Freud et al. 2017), and the seasonality in atmospheric transport patterns (e.g., Stohl 2006). The summer months are marked by high number concentrations of small particles

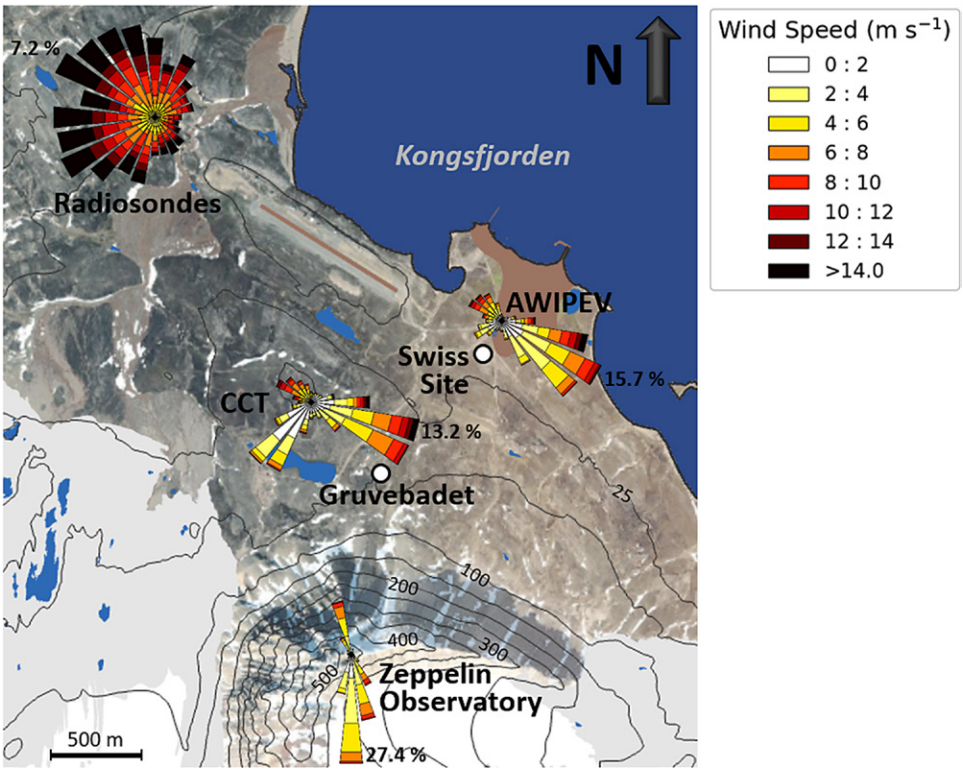

Fig. 4. Wind measurements during NASCENT throughout the Ny-Ålesund area at the different locations and retrieved from radiosondes. Data are shown for the AWIPEV weather mast (10 m), the Zeppelin Observatory, the CCT (10 m), and from daily radiosondes between 3,000 and 3,500 m MSL. The bar length gives the respective frequency of occurrence with the maximum frequency value specified at the end of the longest bar. The topographic map of the Ny-Ålesund region is from Norwegian Polar Institute (2014).

(i.e., with a diameter ≤ 100 nm) due to frequent new particle formation events (e.g., Tunved et al. 2013; Dall'Osto et al. 2017; Beck et al. 2020). In contrast, aerosol mass tends to reach a maximum in the winter and spring months (e.g., Ström et al. 2003) due to long-range transport of pollutants that form the well-known Arctic haze (e.g., Shaw 1995; Quinn et al. 2007). BC concentrations follow the aerosol mass cycle and peak during winter and spring (Eleftheriadis et al. 2009; Sinha et al. 2017).

The typical seasonal cycle of aerosol loading was also observed during NASCENT, as can be seen in Fig. 3, which shows the monthly distributions of daily averaged particle number and BC mass concentrations measured at the Zeppelin Observatory and at Gruvebadet in the valley. The observed aerosol number concentrations (Fig. 3a) at both sites show the same seasonal cycle with a maximum in July and a minimum in the late fall and early winter months, similar to and within a factor of 2 of previous observations (Tunved et al. 2013). This difference, primarily during summer months, can be attributed to different measurement methods: Tunved et al. (2013) used integrated particle number concentrations (using size-resolved measurements), while we used the direct particle concentration measurements using condensation particle counters (CPC) that have a lower particle cutoff diameter and are less influenced by particle diffusion losses.

The BC concentrations were slightly higher in Gruvebadet than at the Zeppelin Observatory, especially throughout 2020, which is most likely due to local emissions from the Ny-Ålesund settlement that impact the Gruvebadet site but not necessarily the mountaintop site, especially during shallow boundary layers (Dekhtyareva et al. 2018; Platt et al. 2022).

As shown in Fig. 3b, the BC levels measured during NASCENT were comparable to values reported previously at the Zeppelin Observatory (Eleftheriadis et al. 2009). For example,

during the pristine summer and autumn, monthly mean BC concentrations at the Zeppelin Observatory amounted only to a few nanograms per cubic meter, which are comparable to values measured over the remote southeast Pacific (Shank et al. 2012) and the Southern Ocean (Schmale et al. 2019).

Clouds. During NASCENT, the monthly cloud cover assessed using the Cloudnet target classification product (Illingworth et al. 2007) ranged between 50% and 85%, out of which 30%–70% had cloud tops below 3 km (Fig. 2b). The low-level cloud occurrence peaked in March 2020 and was at a minimum in December 2019 and January 2020. Liquid-only clouds were primarily observed in the summer and early autumn months. Meanwhile, MPCs and ice clouds were present year-round with ice clouds being the most abundant cloud type except for below 3 km where MPCs were dominant (Fig. 2b). These observations are in accordance with measurements of liquid droplets year-round at the Zeppelin Observatory (Koike et al. 2019). Previous studies investigating cloud cover in Ny-Ålesund have observed similar cloud occurrences albeit with slight differences in seasonality and cloud type contributions (Nomokonova et al. 2019; Gierens et al. 2020). Regardless of this year-to-year variability, MPCs are overall the most prevalent cloud type close to the surface at Ny-Ålesund. This highlights the importance of low-level MPCs year-round in the Arctic region and their potential to alter the Arctic climate.

First research highlights from the NASCENT study

First highlights are described in the following sections to demonstrate how the wide variety of observations contributes to the understanding of properties and interactions of Arctic aerosols and clouds and their subsequent representation in models. We use measurements mainly taken on 12 November 2019 to discuss the role of physical and chemical aerosol properties, cloud droplet activation, ice crystal nucleation, and SIP on the formation and evolution of an MPC, and finish with a comparison of the cloud structure representation in the WRF Model with the in situ cloud observations.

On 12 November 2019, a warm front influenced the weather around Ny-Ålesund (see section S1 and Fig. S1 in the SI). The temperature varied between –3° and 0°C at Ny-Ålesund and between –5° and –3.5°C at the Zeppelin Observatory. A persistent MPC was observed until 2100 UTC, with cloud top rising from 1,300 to 2,000 m MSL and cloud-top temperature varying between –13.5° and –11°C (Fig. S3). The cloud base varied between 200 and 600 m MSL (not show). The large-scale wind measured by the radiosondes (Fig. S7) and visible on the wind lidar measurements above 800 m MSL (Fig. S2) was southwesterly.

Chemical and physical properties of aerosols and cloud residuals. At the Zeppelin Observatory, the cloud particle number concentration (CPNC) and liquid water content (LWC) reached up to 17.5 cm^{-3} and 0.3 gm^{-3}, respectively (Fig. 5a). To assess the size and chemistry of the particles involved in cloud formation, the counterflow virtual impactor (CVI) inlet was used to separate cloud particles from interstitial aerosol. The CVI was in operation for most of the time (Fig. 5b) and the cloud residual number concentration was very low and, as expected, inversely proportional to the visibility (on average ~560 m), which acts as a measure for the optical density of the cloud. The cloud residual size distribution was dominated by small particles of around 10–30 nm (Fig. 5c). These small particles were also present, although to a slightly lower extent, in the whole-air inlet, which samples both interstitial and cloud particles. It is also interesting that the accumulation mode particles (particles between 50 and 200 nm), as measured by the whole-air inlet, were found to a much lower extent within the cloud residuals and thus were probably not CCN and/or INPs at Zeppelin. A possible explanation for this is that the WBF process had occurred and liquid droplets

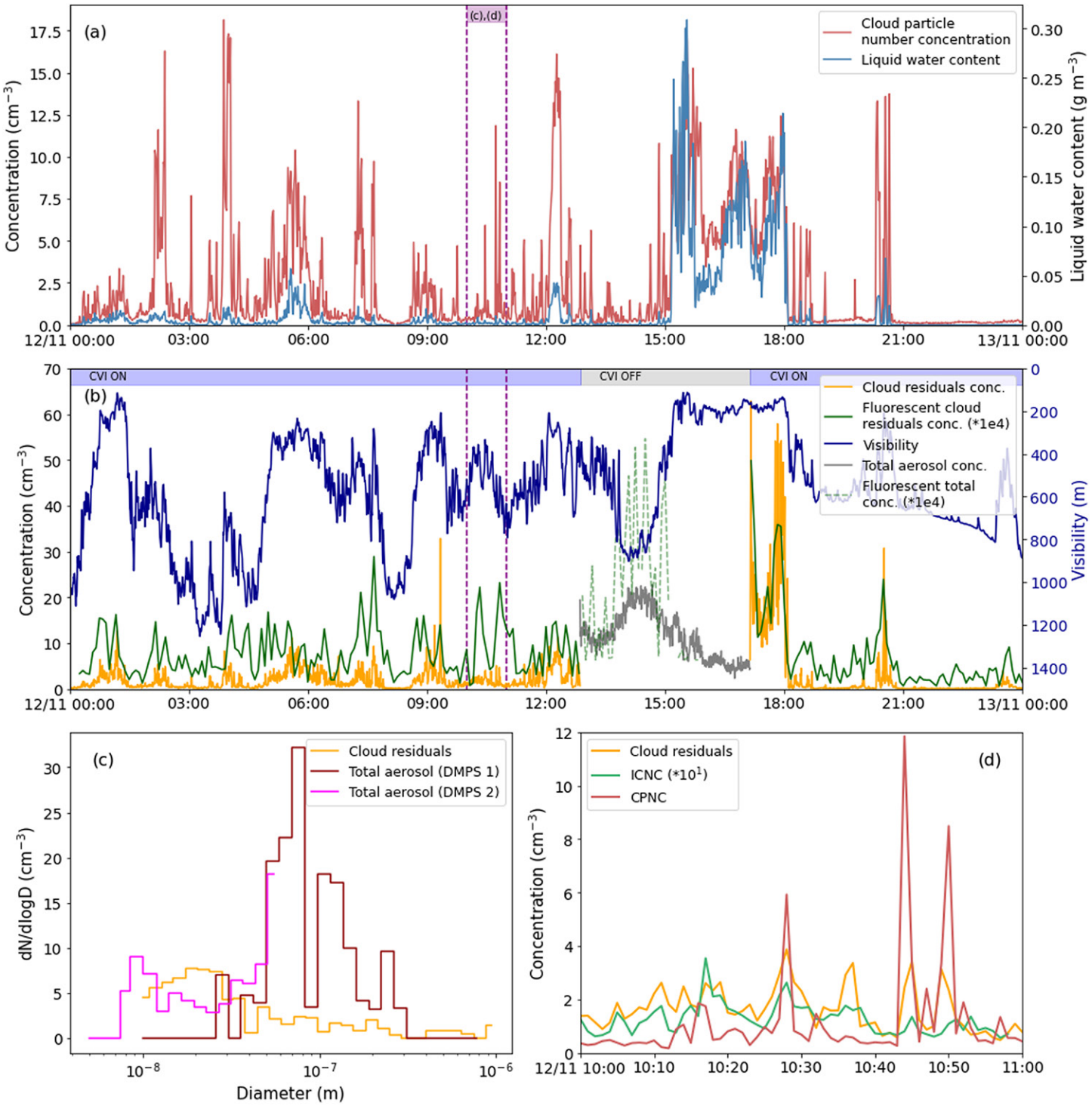

Fig. 5. Cloud in situ measurements on 12 Nov 2019 at Zeppelin Observatory. (a) Cloud particle number concentration and liquid water content measured by the fog monitor. The period shown in (c) and (d) is indicated in purple. (b) Cloud residual number concentration and ambient aerosol number concentration, together with the fluorescent particle concentration (×10⁴) within the cloud residuals/ambient aerosol number concentrations, and ambient visibility measured at the CVI inlet (note the reversed *y* axis). The shading at the top of the figure indicates when the CVI was in operation/ON. (c) Particle number size distribution of the cloud residuals and whole-air aerosols (interstitial and activated aerosol) measured by a tandem-DMPS system. (d) Cloud residual number concentration measured by the CVI inlet, ambient ICNC (×10) measured by HOLIMO3G, and CPNC measured by the fog monitor.

(activated accumulation mode particles) evaporated in the presence of ice, which has been previously observed in MPCs at other mountain sites (Verheggen et al. 2007).

The origin of the enhanced number of small cloud residuals is not fully clear and a number of possibilities (e.g., SIP) and sampling artifacts are discussed in Karlsson et al. (2021). While

previous studies (Karlsson et al. 2021) were missing detailed information on the cloud phase, the holographic imager HOLIMO3G (Beck et al. 2017) allows the determination of ICNC (between 25 μm and 2 mm), and the fog monitor, the determination of CPNC (between 3 and 50 μm) in parallel to the CVI sampling. Even if the exact magnitude of the CVI sampling efficiency still remains to be solved, a good temporal agreement of the ICNC and CPNC with the cloud residual number concentration (Fig. 5d) indicates that sampling artifacts is an unlikely explanation for the small sizes of cloud residuals and suggests that indeed, SIP and the WBF process may cause such small cloud residuals. The cloud residual measurements observed during NASCENT, in combination with the high-resolution cloud probes, will provide new and unique evidence of the importance of sub–accumulation mode particles on cloud formation in the Arctic.

The chemical composition of aerosols, aerosol precursor gases, and cloud residuals at the molecular level was investigated using the FIGAERO-CIMS. On the 12 November 2019, the

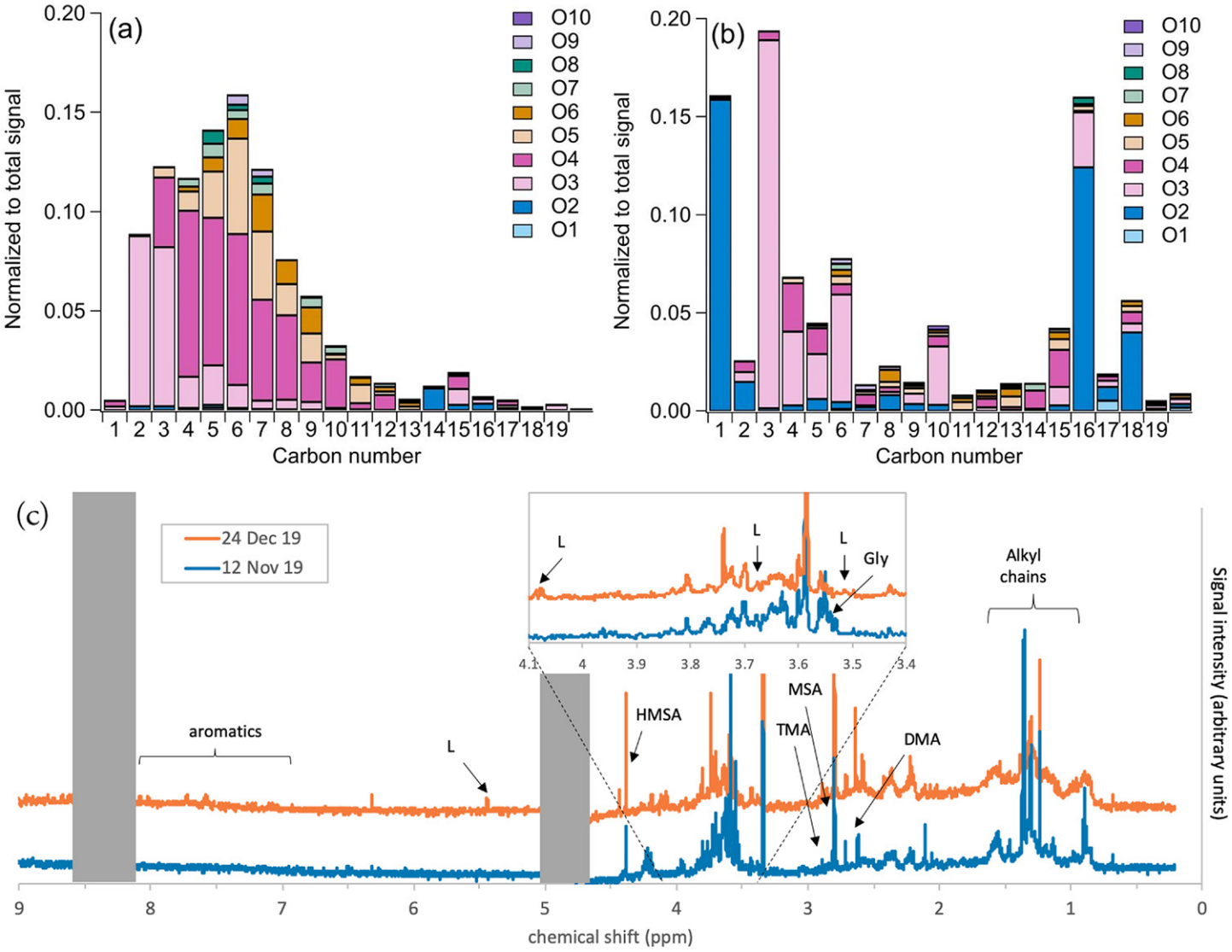

Fig. 6. High-resolution chemical composition of (a) aerosol particles before a cloud event (whole-air inlet) and (b) of cloud residuals during the cloud measured by the FIGAERO-CIMS on 24 Dec 2019. Shown is the background-corrected absolute signal of individual molecules, separated by the number of carbon and oxygen atoms. (c) ^{1}H-NMR spectra of ambient PM1 samples collected at Gruvebadet for 12 Nov and 24 Dec 2019. Specific resonances are assigned to levoglucosan (L), hydroxymethane-sulfonic acid (HMSA), methane-sulfonic acid (MSA), dimethylamine (DMA), trimethylamine (TMA), and glycerol (Gly). Unresolved mixtures of aromatic compounds and linear aliphatic chains, including possible contributions from lipids, are indicated in the spectra. The insert provides a focus on the aliphatic region of the spectra characteristic of polyols/saccarides compounds (H-C-O). Gray areas between 4.7 and 5.0 ppm and between 8 and 8.5 ppm cover the disturbance due to solvent and buffer solutions needed for the analysis.

instrument only sampled the gas phase. Therefore, to illustrate the capability of this analytical tool for the aerosol particle phase, here we present an example from 24 December 2019. On this day, a low-level MPC (cloud top below 2 km) was observed, and the ground temperatures varied between −9° and −6°C at Ny-Ålesund. Figures 6a and 6b show a comparison of the chemical composition of aerosol particles before a cloud event to aerosol particles that were activated as INPs or CCN (cloud residuals). The ~400 organic compounds identified in the particle phase by FIGAERO-CIMS are grouped based on their number of carbon and oxygen atoms, and the signal of groups with the same carbon numbers are stacked. To our knowledge, this is the first time that such a detailed chemical analysis is shown for Arctic cloud residuals.

Molecules with up to 20 carbon atoms and 10 oxygen atoms were identified in both the precloud aerosol and cloud residuals. The majority of the precloud aerosol mass was from compounds with up to 10 carbon atoms. A prominent contribution from $C_6H_{10}O_5$, likely levoglucosan, a marker for biomass burning emissions, was observed. This indicates long-range transport of pollution from wintertime solid fuel combustion on the Eurasian continent as a potential source for particle components observed here. However, the biomass burning chemical signature was not observed in the cloud residuals. The cloud residual chemical composition showed relatively smaller contributions of compounds with up to 10 carbon atoms and more than 5 oxygen atoms (see Fig. 6), and relatively higher contribution of compounds with larger carbon chains and 2 oxygen atoms, potentially fatty acids. These first results could indicate that the organic fraction relevant for cloud formation in the Arctic consists of molecules with rather long carbon chains, at least in the winter months.

Simultaneous measurements of organic aerosol chemical composition via H-NMR from ambient PM1 filter samples at Gruvebadet on 24 December 2019 are qualitatively comparable to those of the FIGAERO-CIMS at the Zeppelin Observatory. In particular, as highlighted in Fig. 6c, the H-NMR confirms the presence of levoglucosan and aromatic compounds (e.g., phenols and methoxyphenols), further supporting the possible long-range transport of biomass burning emissions from the continents. This feature is common during the winter season (Zangrando et al. 2013; Feltracco et al. 2020). These samples are also impacted by high contributions of hydroxymethane-sulfonic acid (HSMA), a product of the atmospheric oxidation of formaldehyde and considered a tracer for anthropogenic emissions. In contrast, there is no evidence for biomass burning influence on the filter sample from the 12 November, which instead has an NMR spectral fingerprint more typical of

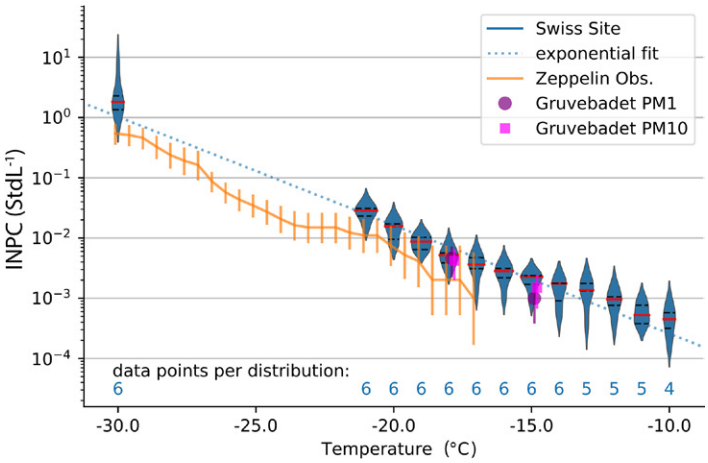

Fig. 7. Overview of INPCs observed on 12 Nov 2019. Blue violin plots: six INP samples measured with the Droplet Ice Nuclei Counter Zurich (DRINCZ; David et al. 2019; Wieder et al. 2022b) between −10° and −21°C and with the Horizontal Ice Nucleating Chamber (HINC; Lacher et al. 2017) at −30°C at the Swiss site. The red lines indicate the median and the dashed black lines the 25th and 75th percentiles. The blue dashed line shows the corresponding exponential fit [INPC(T) = exp(−0.4146T − 12.4059) (cf. Li et al. 2022)]. Purple and magenta: one filter sample collected between 0900 and 1200 UTC at Gruvebadet analyzed by the Dynamic Filter Processing Chamber (DFPC; Santachiara et al. 2010; Rinaldi et al. 2017) on PM1 and PM10. Orange line: one filter sample collected from 10 to 16 Nov 2019 at the Zeppelin Observatory analyzed by the Cryogenic Refrigerator Applied to Freezing Test (CRAFT; Tobo 2016; Tobo et al. 2019, 2020). The error bars represent the 95% confidence interval.

background clean and marine influenced environments. It contains marine biogenic tracers like glycerol, methane-sulfonic acid (MSA), amines (DMA and TMA in particular) and alkylic chains, potentially attributable to lipids from marine biota. The presence of possible fatty acid alkylic chains, which were also observed on the 24 December sample, and found by FIGAERO-CIMS in the cloud residuals, suggests that marine aerosol contributes to Arctic cloud formation, but this needs to be further investigated.

Future work will shed further light into the importance of the WBF process and SIP throughout the seasons. In addition, the role of particle and gas phase chemistry and the role of biological particles in cloud formation is being investigated.

Ice nucleating particle concentrations. INP measurements were conducted at the Swiss site with HINC and DRINCZ, at the Zeppelin Observatory with CRAFT, and at Gruvebadet with DFPC. Despite the different techniques used, the INPCs as a function of temperature measured by the four methods agree within a factor of around 5 (Fig. 7). This is substantial for a highly spatiotemporally varying quantity such as INPs, which occur at very low concentrations. The observed INPC ranged from ~2 $StdL^{-1}$ at −30°C down to the lowest detectable concentration of ~10^{-4} $StdL^{-1}$ at −10°C. While there is agreement between the INPCs measured in the overlap temperature range (from −21° to −15°C), on average the INPCs obtained at the Zeppelin Observatory are slightly below those measured at Gruvebadet and at the Swiss site (Fig. 7). This is likely because the Zeppelin Observatory experiences less local influence from the boundary layer and from the town of Ny-Ålesund (Platt et al. 2022) (see Fig. 8a). Moreover, the CRAFT measurements represent the INPCs averaged over three days, while at the Swiss site INPCs were measured at higher frequency (10 to 40 min averages). The use of two different filter cutoff sizes (PM1 and PM10) gives some information about the size of the INPs. At −18°C (−15°C) the INPC retrieved from the PM10 filter were 10% (50%) higher than

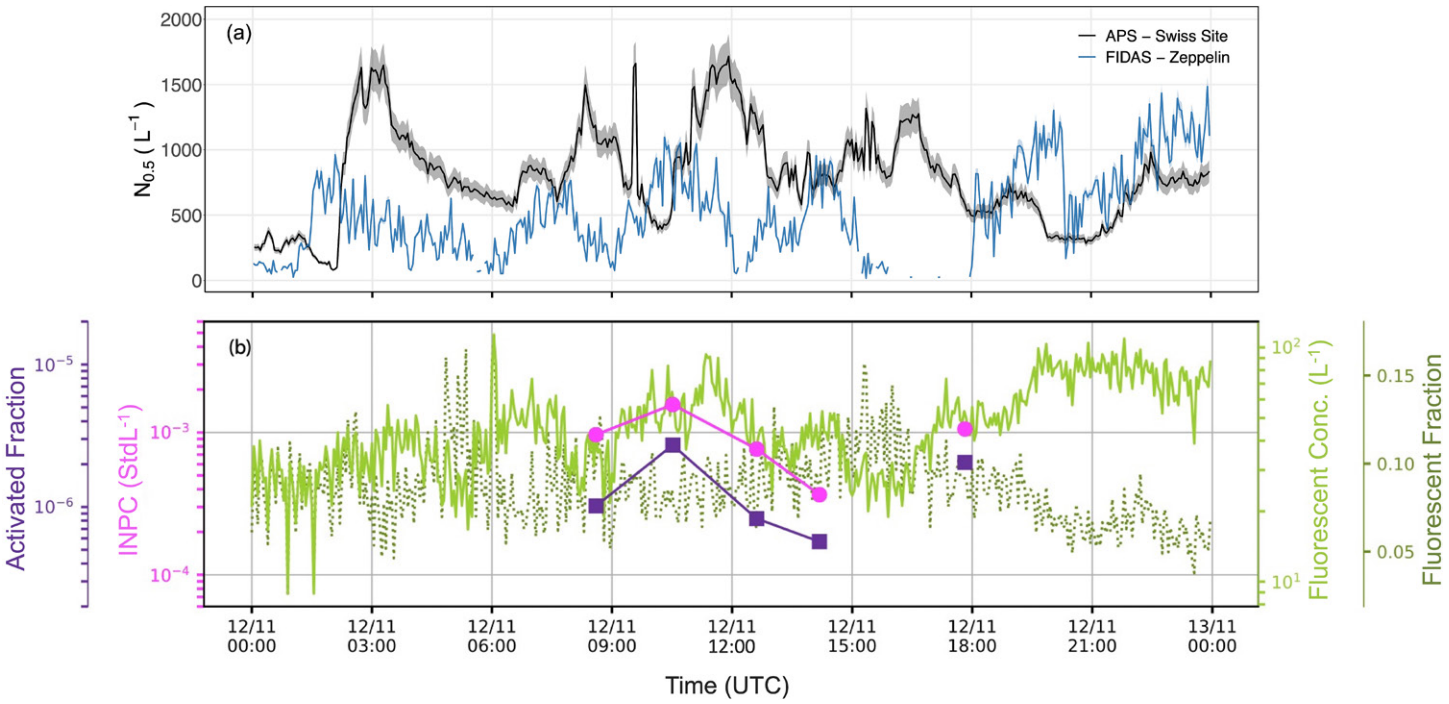

Fig. 8. (a) Particle number concentration for sizes ≥ 0.5 μm measured by the APS (aerodynamic diameter) at the Swiss site and by the FIDAS (optical diameter) at the Zeppelin Observatory, with a time resolution of 3 min for both instruments. (b) INPC and activated fraction (INPC/$N_{0.5}$) at −12°C (left axis), and fluorescent (particle) concentration and fluorescent (particle) fraction (right axis). We select a temperature of −12°C to adequately evaluate the contribution from biological aerosol particles (Kanji et al. 2017, and references therein). The INPCs are measured by DRINCZ and the fluorescent particle concentration by a Wideband Integrated Bioaerosol Sensor (WIBS). The fractions are normalized to the particle fraction ≥ 0.5 μm.

the one retrieved from the PM1 filter (squares and circles in Fig. 7). This difference suggests that the observed INPs at −15°C were larger than 1 μm and smaller than 10 μm whereas the observed INPs at −18°C were smaller than 1 μm. This size dependence is consistent with previous studies (e.g., Mason et al. 2016) and highlights the importance of supermicron aerosol on ice formation at temperatures above −15°C.

For most of the day, higher aerosol concentrations (≥0.5 μm) were measured at the Swiss site than at the Zeppelin Observatory and an inverse trend in concentrations is observed at the two sites (Fig. 8a). Only between 0300 and 0600 UTC and from 2000 UTC onward do the aerosol concentrations follow the same trend. Previous field measurements have suggested that biological particles are a key source of INPs in the Arctic (e.g., Bigg and Leck 2001; Tobo et al. 2019; Hartmann et al. 2020). Therefore, the contribution of biological particles as INPs is investigated via the fluorescent aerosol concentration and fraction at the Swiss site. The fraction of fluorescent aerosol was not constant throughout the day, which implies that the fluorescent particles did not always scale with aerosol concentrations ≥ 0.5 μm (Fig. 8b). Rather the fluorescent aerosol made up a variable subset of the total aerosol population ≥ 0.5 μm, which likely had a myriad of sources. However, consistent with previous observations, the INPC and activated fraction at −12°C, follow the same trend as fluorescent aerosol concentration (Fig. 8b). This relationship suggests a correlation between the fluorescent particle concentrations and the observed INPC and INP activated fraction and, therefore, provides additional evidence that biological particles could play an essential role in controlling cloud phase in the Arctic (Creamean et al 2022; Carlsen and David 2022). Further analysis will be conducted to determine if INPC parameterizations based on biological particles should be used to accurately represent ice formation in Arctic clouds (Burrows et al. 2022).

Cloud microphysical properties. Three flights into clouds were performed with HoloBalloon on 12 November 2019 (Fig. S3). Here we focus on the cloud microphysical measurements taken with HOLIMO3B on HoloBalloon and the cloud radar between 1445 and 1630 UTC (Fig. 9), together with the INP and CCN measurement to identify the processes responsible for ice crystal and cloud droplet formation.

During the entire flight, HOLIMO3B measured CDNCs between 5 and 15 cm^{-3} and a mean diameter of ~30 μm (Fig. 9c). Drizzle drops with diameter larger than 56 μm contributed to this large mean diameter (Figs. 9c,e). In comparison, continental clouds typically have higher CDNC (40–1,000 cm^{-3}) and a smaller mean diameter (8 μm) (Lohmann et al. 2016). Aerosol particles with dry diameters larger than 70 nm measured by a differential mobility particle sizer (DMPS) at the Zeppelin Observatory were used as a proxy for the CCN concentration, following the method described by Koike et al. (2019). The estimated CCN concentration between 1000 and 1700 UTC was ~9 cm^{-3} (not shown) and was comparable to the CDNCs measured by HOLIMO3B. This indicates that the cloud droplet formation was limited by the CCN availability and is in accordance with previous studies showing that CDNC is sensitive to CCN concentration in aerosol-limited pristine regions (e.g., Reutter et al. 2009; Moore et al. 2013).

During the first part of the flight (1445–1545 UTC), the mean Doppler velocities at the altitude of HoloBalloon were rapidly varying with time, even though the reflectivities remained less variable and HoloBalloon flew approximately at a constant altitude (Figs. 9a,b). This indicates a turbulent atmosphere, which is in accordance with the observed veering of the wind near the altitude of HoloBalloon (Fig. S3). This turbulence and updrafts favored the formation of the drizzle drops observed by HOLIMO3G (Figs. 9c,e) (Ramelli et al. 2021). During the second part of the flight (1545–1620 UTC), a fall streak pattern is visible in the increased reflectivity measured by the cloud radar (≥10 dBZ). As these two periods are quite

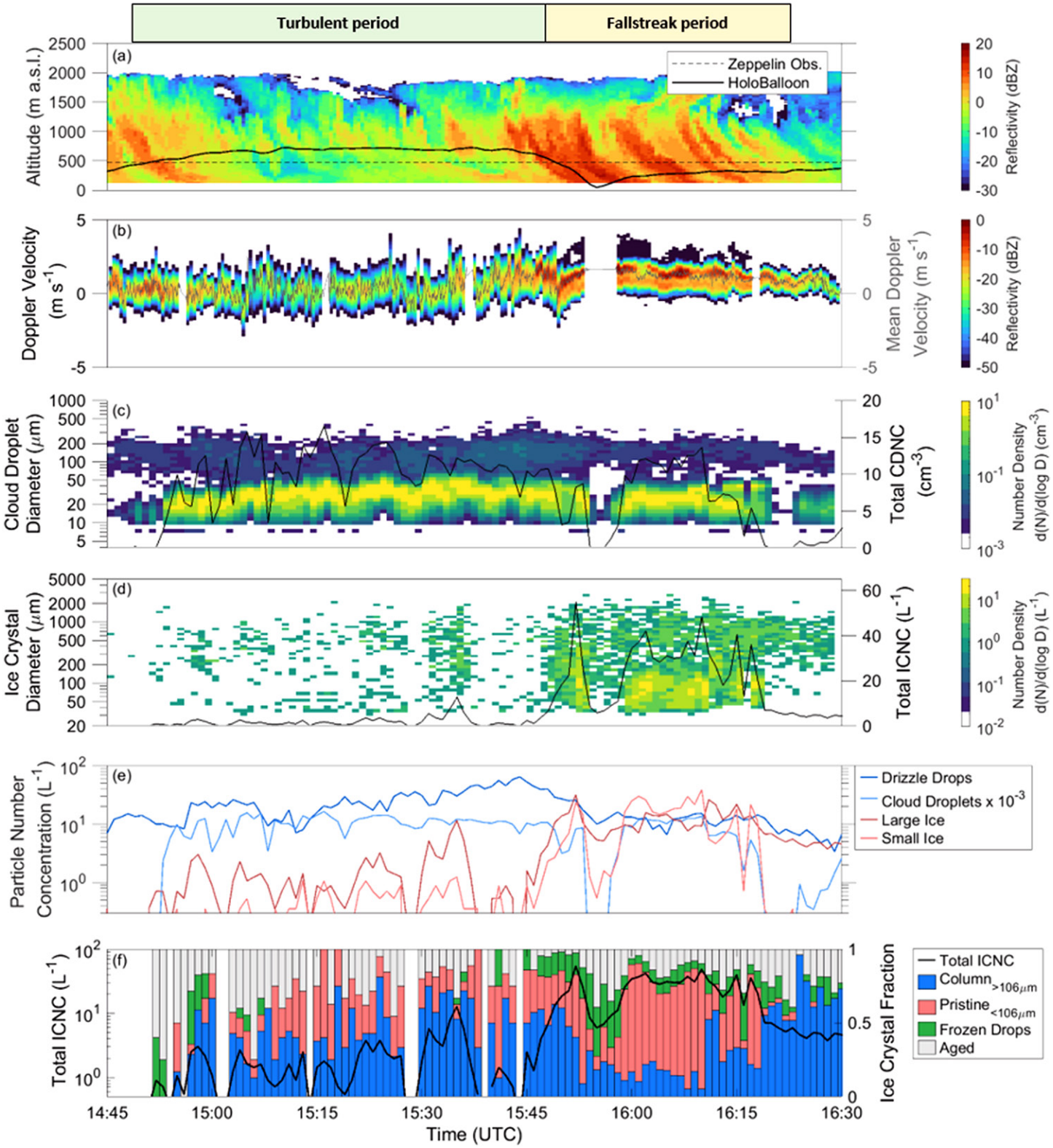

Fig. 9. Overview of the cloud properties observed in situ on HoloBalloon and by the cloud radar on 12 Nov 2019. (a) Cloud radar reflectivity, HoloBalloon path, and Zeppelin altitude. (b) Doppler spectra and mean Doppler velocity at the height of the HoloBalloon path. Positive values represent a downward velocity. (c) Cloud droplet and (d) ice crystal size distributions (color) and total CDNC and ICNC (black line) measured by HOLIMO3B. (e) Cloud droplets, drizzle drops, and ICNC for crystals smaller and larger than 106 μm. This cutoff size is defined by the bin size closest to 100 μm. (f) Frequency of occurrence of the ice crystal habits and total ICNC. The data are averaged over 60 s. Note that at around 1550 UTC, HoloBalloon flew out of the cloud, which explains the decrease in CDNC and ICNC measured by HOLIMO3B in (c)–(f) and the missing reflectivity data at the HoloBalloon height in (b).

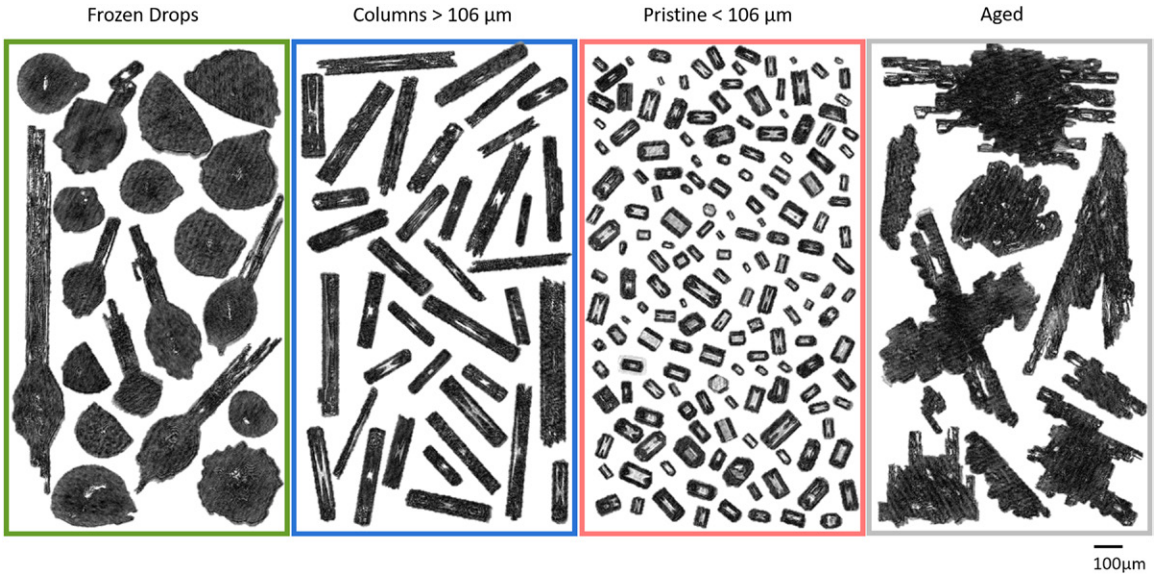

Fig. 10. Examples of ice crystals classified as typical habits observed with HOLIMO3B. Plates and (hollow) columns with a diameter smaller than 106 μm were classified as pristine, whereas larger columns were classified separately. Droplet "lollipop" and drops showing evidence of freezing are classified as frozen drops. All the other ice crystals, including rimed and aggregated particles are classified as "aged." The scale bar in the right panel is representative for all of the panels. The respective fractions of the typical ice crystals habits to the total ICNC are displayed in Fig. 9f.

distinct from each other, we refer in the following to the *turbulent period* (1445–1545 UTC) and the *fall streak period* (1545–1620 UTC).

Here we consider the fall streak period in detail. HOLIMO3B measured an increase in total ICNC from below 0.5 L^{-1} up to 55 L^{-1} (Fig. 9d). Large ice crystals (diameters ≥ 106 μm) consisting of columns, frozen drops, and aged particles, as well as small pristine ice crystals (diameters ≤ 106 μm) contributed to this increase (Figs. 9e,f). Between 1600 and 1610 UTC, the concentration of small pristine ice crystals reached up to 40 L^{-1} and was greater than the concentration of larger ice crystals (Figs. 9e,f). Note that the influence from ice crystals from the ground (e.g., blowing snow) can be neglected as HoloBalloon flew up to ~700 m above the surface. A representative set of (hand-labeled) pictures of ice crystals contributing to the total ICNC as shown in Fig. 9f are displayed in Fig. 10. Whereas the large ice crystals likely originated from higher portion of the clouds, the small pristine ice crystals must have formed close to the measurement location of HoloBalloon, as ice crystals grow rapidly in the water saturated environment (Korolev et al. 2020). In the temperature regime of the HoloBalloon measurements (between −8° and −1°C), the INPCs were below the instrument detection limit (no data in Fig. 7) and at cloud-top temperatures (from −13.5° to −11°C), the INPCs were on the order of ~10^{-3} $StdL^{-1}$. As such, primary ice nucleation due to INPs acting in the immersion mode alone can neither explain the concentration of larger ice crystals originating from close to cloud top, nor the concentration of small ice crystals formed close to the measurement location of HoloBalloon. Therefore, we deduce that SIP enhanced the formation of the ice crystals in higher parts of the cloud and that SIP close to the measurement location was responsible for the sudden increase in concentration of small pristine ice crystals observed.

Our interpretation is that the primary ice was formed aloft where the cloud temperature was lower and thus more INPs were present. Then, SIP increased the ICNC near cloud top and the ice crystals grew until they were heavy enough to overcome the updrafts. As they fell, they continued to grow as columns (Fig. 10), consistent with the ambient temperature experienced, until they reached the altitude of HoloBalloon, as indicated by the higher radar reflectivities with decreasing altitude in the cloud (Fig. 9a). The columns then collided with drizzle

drops, producing the observed "ice lollipops" (Fig. 10) consisting of frozen drizzle drops and columns (Keppas et al. 2017). Such ice lollipops were also observed by HOLIMO3G and the Hawkeye Probe at the Zeppelin Observatory (Fig. S6). Upon collision and freezing, the drizzle drops likely created splinters through droplet shattering (e.g., Lauber et al. 2018; Korolev and Leisner 2020). Laboratory experiments have shown that the number of ice splinters produced from a single drop freezing can reach up to 200 (Korolev and Leisner 2020). The splinters produced during the freezing of the drizzle drops then grew to the small columns observed by HOLIMO3B. These small columns could in turn collide with drizzle drops, initiate their freezing, and the formation of additional ice splinters. We suggest that this can lead to a cascading SIP process explaining the rapid increase in concentrations of small ice crystals observed, similarly to the study by Lawson et al. (2015).

Our findings on SIP are in agreement with other studies. First, the occurrence of SIP with low INPC (10^{-4} and 0.01 L^{-1}) was already observed in a study by Lawson et al. (2015). Second, a difference of up to four orders of magnitude between the INPC and ICNC are consistent with previous observations (e.g., Ladino et al. 2017; Li et al. 2021; Wieder et al. 2022a). Finally, a recent study using remote sensing techniques showed that droplet shattering was a more efficient SIP process than the rime-splintering process at slightly supercooled temperature in Arctic MPCs (Luke et al. 2021).

Next we demonstrate how the combination of the cloud radar and in situ measurements complement each other to evaluate the microphysical properties of the observed MPC using the Passive and Active Microwave radiative Transfer tool (PAMTRA; Mech et al. 2020). PAMTRA simulated the cloud radar Doppler spectra based on the ice crystal and cloud droplet size distributions measured by HOLIMO3B (Fig. 11). The variety of ice crystal habits were described by three categories (small ice, large ice, and frozen drops). More information about the PAMTRA settings is provided in the SI. Three representative time periods are compared (Fig. 11): 1) during the turbulent period (1525–1530 UTC) with cloud droplets, drizzle drops, and a low concentration of ice crystals, 2) during the fall streak period (1600–1605 UTC) with

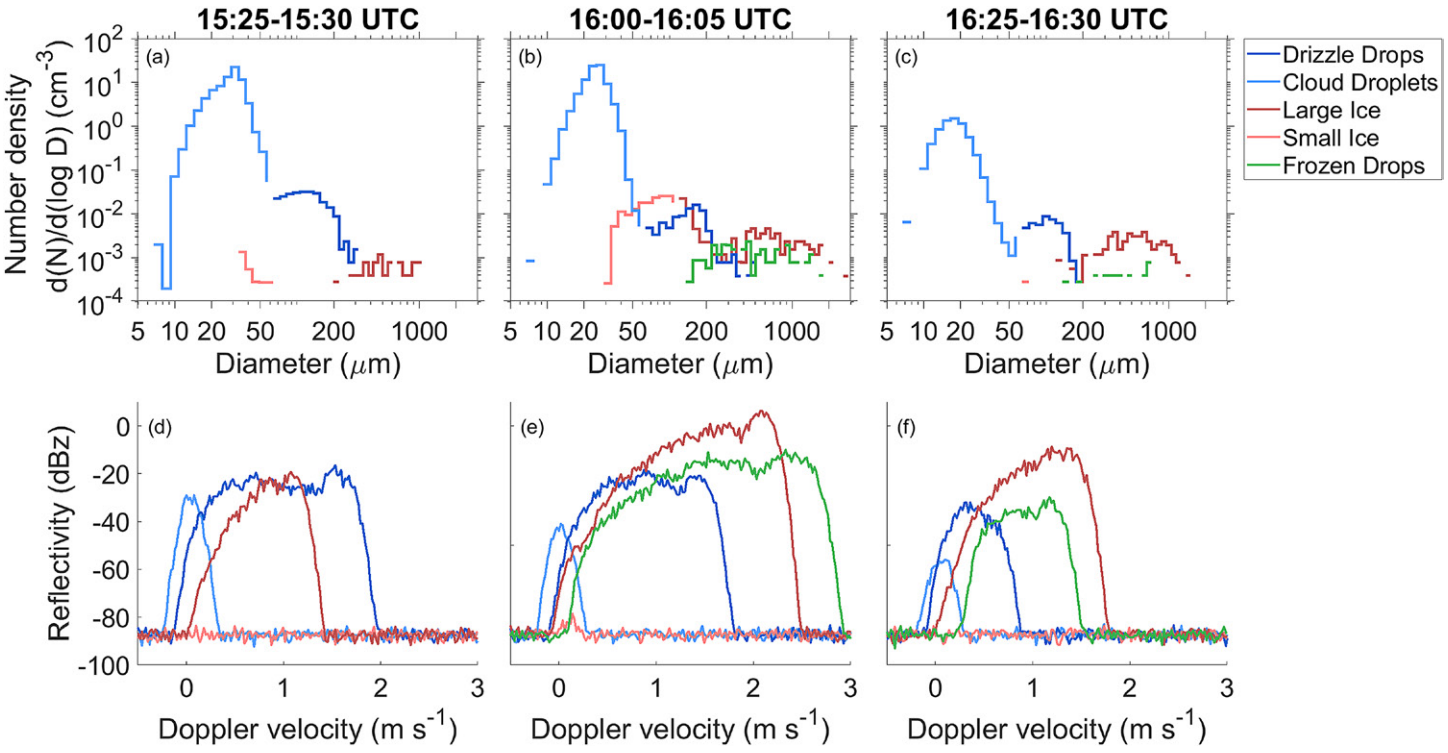

Fig. 11. (a)–(c) Measured size distributions from HOLIMO3B. (d)–(f) Radar Doppler spectra simulated with the PAMTRA tool using the size distribution shown in (a)–(c). The measured size distribution and simulated Doppler spectra are shown at three characteristic time periods of 5 min: (left) 1525–1530 UTC, (center) 1600–1605 UTC, and (right) 1625–1630 UTC.

frozen drops and a higher concentration of ice crystals, and 3) during the period afterward (1625–1630 UTC) with low concentration of cloud droplets and drizzle drops.

We start by allocating parts of the Doppler spectra signal to the different hydrometeor types. In the PAMTRA simulations, large ice crystals were generally responsible for the higher reflectivities (up to 5 dBZ) with fall velocities between 0 and 2.5 m s^{-1} (Figs. 11e,f). This is due to the strong dependence of reflectivity on particle size (Doviak and Zrnić 2006). Meanwhile, the measured frozen and drizzle drops were responsible for the simulated reflectivity at large fall velocities (up to 3 m s^{-1}) (Fig. 11e) and for the lower reflectivity (up to –20 dBZ) with fall velocities up to 2 m s^{-1} (Figs. 11d–f), respectively. Finally, measured cloud droplets and smaller ice crystals (diameter ≤ 100 μm) were only responsible for reflectivities below –30 and –80 dBZ, respectively, and fall velocities around 0 m s^{-1}.

Applying these results to the cloud radar measurements along the HoloBalloon path during the fall streak period (Fig. 9b), we find that the higher reflectivities with Doppler velocities of around 1 m s^{-1} (Fig. 9b) were produced by large falling ice crystals, whereas observed reflectivities below –40 dBZ and fall velocities between 2 and 4 m s^{-1} were generated by frozen drops, as only these particles have such high fall velocities and low reflectivity (Fig. 9b). The reflectivity between –30 and –10 dBZ at Doppler velocities around 0 m s^{-1} indicates the presence of small ice crystals, and possibly cloud droplets when reflectivities are at the lower side (below –17 dBZ; see, e.g., Kogan et al. 2005). Nevertheless, when looking at the PAMTRA simulations during the turbulent time periods, it can be difficult to distinguish the contributions of different hydrometeors to the Doppler spectra. Indeed, the reflectivity and fall velocity of drizzle drops and large ice crystals overlap and the drizzle drops are responsible for the highest reflectivities and fall velocities (Fig. 11d). The combination of the information obtained by HOLIMO3B and by the Doppler spectra is thus complementary and help to gain a better understanding of the microphysical processes in Arctic MPCs.

Model comparison. To understand how the representation of clouds can be ameliorated in weather and climate models, we compared the cloud properties simulated by the regional WRF Model with the in situ cloud measurements. To represent the microphysics we used the double-moment scheme developed by Milbrandt and Yau (2005), which has six classes for cloud water, ice, rain, snow, graupel, and hail. The CCN concentration was prescribed as 9 cm^{-3} based on the concentration of aerosols > 70 nm (Koike et al. 2019) and the INPC was prescribed based on the exponential fit of the INPC measurements on 12 November shown in Fig. 7. The simulated meteorological conditions were validated against the radiosonde observations (Fig. S7). Further information about the model setup is given in the SI.

The data were averaged for each flight time period to compare the observed and simulated cloud properties. Additionally, to match the acquisition by HOLIMO3B, the simulated cloud droplets and drizzle/rain drops were merged into one category to obtain the total LWC and liquid droplet number concentration (LDNC). The same was done for simulated small cloud ice and larger precipitating ice crystals (snow, hail, graupel) to obtain total ice water content (IWC) and ICNC.

The model correctly simulated an increase in the cloud-top height from flight 1 to 3 as measured by the cloud radar (Fig. S9). Also, the cloud-base height derived from the simulated hydrometeor populations follows the development indicated by the ceilometer measurements (Fig. S9). Hereafter we focus on flight 3, when HOLIMO3B observed substantial SIP to assess how well the model reproduces ice production in Arctic MPCs (Fig. 12). Generally, the simulation is in agreement with the observations as the LDNC and LWC are consistent with the maximum values measured by HOLIMO3B between 600 and 750 m MSL, albeit at altitudes between 1,000 and 1,500 m MSL. Below the simulated cloud base (~600 m MSL), the simulation underestimates the LDNC and LWC. This may be the reason for the sharper decrease in

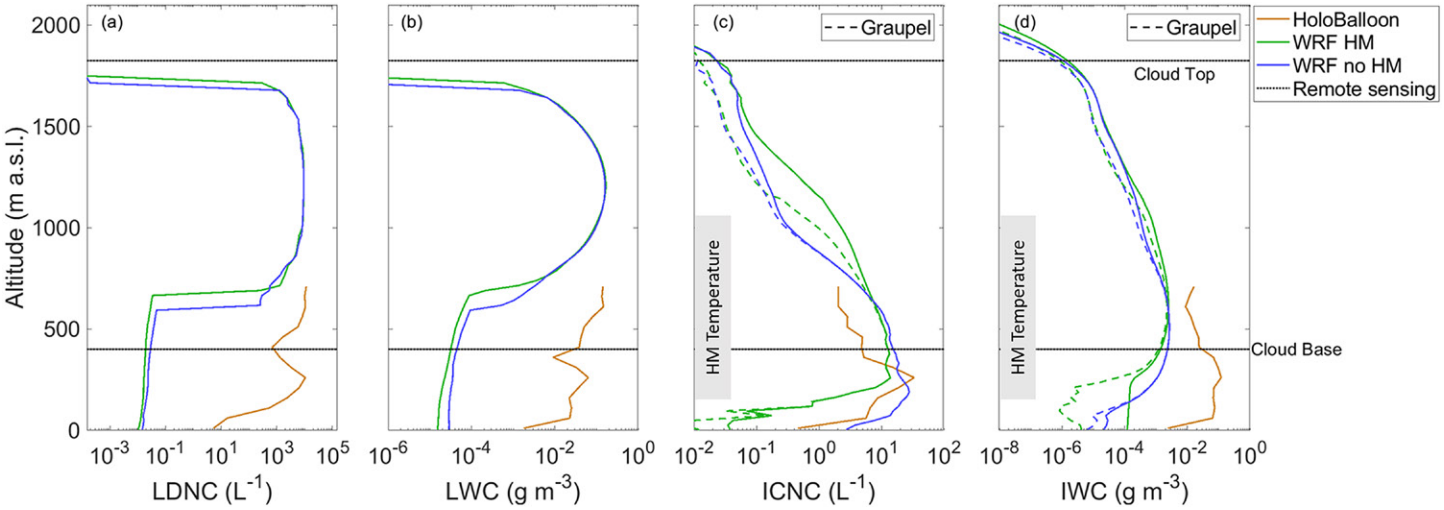

Fig. 12. The averaged vertical profiles during flight 3 on 12 Nov 2019 observed by HOLIMO3B and simulated by WRF. (a) LDNC, (b) LWC, (c) ICNC, and (d) IWC. The contribution of graupel to the ICNC and IWC are shown with the colored dashed profile line in (c) and (d). The data from HOLIMO3B are averaged over 50-m altitude bins and the WRF data over every model layer. The average cloud base and cloud top measured by the remote sensing instrumentation (ceilometer and cloud radar, respectively) are represented by the black dotted horizontal lines and the HM temperature range (from –8° to –3°C) is highlighted in (c) and (d).

the simulated ICNC and IWC than in the observed ones below 300 m MSL. Regardless, the simulation reproduces the maximum concentrations of ICNC and IWC observed by HOLIMO3B during flight 3, but the principal constituent of the simulated ICNC and IWC is graupel, which was not observed by HOLIMO3B (see Figs. 9f and 10). The ability for the simulation to reproduce the observed ICNC is surprising considering that the prescribed INPC at cloud top (~10^{-3} L^{-1}) is approximately four orders of magnitude lower than the observed and simulated ICNC. The Milbrandt and Yau scheme (Milbrandt and Yau 2005) includes SIP via the Hallett–Mossop (HM) process (Hallett and Mossop 1974), which could potentially improve the models ability to accurately predict the ICNC, especially as a significant fraction of the cloud falls within the temperature range relevant for the HM process (Figs. 12c,d). To determine if the HM process is responsible for the realistic ICNC simulated, we conducted the simulation again without the HM process activated. The ICNC decreases above ~800 m when the HM process is deactivated (Fig. 12). However, below this height, the model still simulates ICNCs that exceed the maximum ICNC when the HM process is active. This indicates that the microphysics scheme is producing ice independently of HM being active in the simulations. This may partly be due to the Milbrandt and Yau scheme lacking a sink term for INPC, which has been recommended to prevent models from nucleating ice continuously (Kärcher and Marcolli 2021). Regardless, the production of graupel by the model when none was actually observed, indicates that the simulations fail to accurately represent the formation and evolution of ice in Arctic MPCs.

To conclude, the simulation is able to qualitatively represent the structure of the cloud, including the cloud-top and cloud-base heights when the correct CCN and INP concentrations are prescribed. It also represents the realistic ICNC during flight 3 but for the wrong reasons. This indicates that the Milbrandt and Yau scheme has inconsistencies in the formation of ice hydrometeors and in particular, graupel, in the presence of very low CCN and INP concentrations representative of the Arctic. Future work will utilize the in situ aerosol and cloud microphysical measurements as well as the remote sensing observations to address this inconsistency and develop and validate parameterizations for the SIP observed.

Summary and future work

The Ny-Ålesund Aerosol and Cloud Experiment (NASCENT) was initiated to improve our understanding on how aerosols, clouds, and their interactions influence the Arctic climate. A comprehensive set of cloud, aerosol, and meteorological observations was obtained over the course of one year, which included detailed in situ and remote sensing techniques on ground-based and airborne platforms. Regarding the atmospheric seasonality, the mean temperature between December 2019 and April 2020 was substantially colder than the climatology (up to 6°C) due to a strong polar vortex, whereas the summer 2020 was slightly warmer than usual. The wind speed and direction were strongly influenced by the surrounding topography as found in previous studies. Aerosol particles, such as BC particles, followed the typical aerosol mass cycle found on Svalbard, with maximum concentrations during winter and spring. MPCs were the most abundant low cloud type during NASCENT. This high frequency highlights their importance for the Arctic climate.

We present first highlights from NASCENT by showing a detailed case study and discuss how in situ observations of aerosols and clouds, together with remote sensing instrumentation and modeling can be combined to better understand the aerosol and cloud microphysical processes related to Arctic MPCs.

The cloud residuals measured by the CVI inlet were in good temporal agreement with measurements taken by two cloud probes at the Zeppelin Observatory. The measurements also revealed clear differences in molecular composition between ambient aerosol particles and those particles that were involved in cloud formation and evidence was found that biological particles acted as INP at warm temperatures. In future work, our dataset will be used to further examine the composition and physical properties of cloud residuals and ambient aerosols and their role and fate during cloud formation. Furthermore, a parameterization for estimating the INPC in the Arctic is under development.

Using aerosol in situ measurements and vertical cloud profiling with the tethered balloon system HoloBalloon, we found that the cloud droplet formation was limited by the available CCN concentration. Regarding the cold cloud processes, we showed that INPC could not explain the measured ICNC. Instead, frozen drops, followed by an increase in small pristine ice crystals were observed and provide evidence for the occurrence of SIP via droplet shattering. Further measurements of the HoloBalloon system are being analyzed together with remote sensing observations to constrain the required conditions for different SIP processes in Arctic MPCs.

First modeling results with the WRF Model have shown that the model is able to simulate the cloud structure and simulates a representative ICNC probably for the wrong reasons. In future work, more SIP parameterizations will be tested and compared to the measurements with HoloBalloon to ameliorate the representation of clouds in weather and climate models and to understand how they influence the radiative fluxes in the Arctic climate.

The NASCENT study has acquired a unique and holistic set of observations that will contribute to improve our understanding of aerosol and cloud processes in the Arctic. Together with further in-depth analysis and modeling studies, this work will help to clarify their role in the observed Arctic amplification and the Arctic climate system in general.

Acknowledgments. This project has received funding from the European Union's Horizon 2020 research and innovation programme under Grant Agreement 821205 (FORCeS), from the Swiss Polar Institute (Exploratory Grants 2018), and from the Swiss National Science Foundation (SNSF) (Grant 200021_175824). We gratefully acknowledge the funding by the European Research Council (ERC) (Grant StG 758005) and the Deutsche Forschungsgemeinschaft (DFG; German Research Foundation)–Project-ID 268020496–TRR 172, within the Transregional Collaborative Research Center "Arctic Amplification: Climate Relevant Atmospheric and Surface Processes, and Feedback Mechanisms (AC)³."

We are thankful for funding support from Knut and Alice Wallenberg (KAW) foundation financed projects Arctic Climate Across Scales (ACAS; Project 2016.0024) and WAF project CLOUDFORM, Grant 2017.0165, Swedish environmental protection agency (Naturvårdsverket), the Swedish Research Council (Vetenskapsrådet starting grant, Project 2018-05045) and FORMAS agency funded project "Interplay between water vapor, clouds and aerosols in the Arctic." This project was supported by the Environment Research and Technology Development Fund (JPMEERF20202003) of the Environmental Restoration and Conservation Agency of Japan, and the Ministry of Education, Culture, Sports, Science, and Technology (MEXT) in Japan (ArCS II Project, JPMXD1420318865) and JSPS KAKENHI (Grants JP18H03745, JP18KK0292, JP19K14802, JP19H01972). This project was supported by the Korea Polar Research Institute (PE21010). We gratefully acknowledge funding from an access grant provided by the Research Council of Norway, Project 291644, Svalbard Integrated Arctic Earth Observing System–Knowledge Centre, operational phase. This research was also supported by EEARO-NO-2019-0423/IceSafari, Contract 31/2020, under the NO grants 2014–2021 of EEA Grants/Norway Grants. We thank Rafael Tazima (Brazil) for helping in designing our NASCENT logo of a polar bear studying the "nascency" of an Arctic cloud droplet. We thank Davide Ori for his precious help regarding the PAMTRA simulations. We owe great thanks to all technicians and helpers involved in the field work associated with NASCENT, particularly the AWIPEV and Norwegian Polar Institute Sverdrup stations staff. Finally, we thank two anonymous reviewers for their constructive and helpful feedback on the manuscript, which strengthened the paper

Data availability statement. The data and metadata of NASCENT study will be available on the Bolin Centre Database (https://bolin.su.se/data/) using the keyword "NASCENT." Data from AWIPEV (e.g., radiosounding, wind lidar, ceilometer, and cloud radar data) are available in PANGAEA (www.pangaea.de). The Cloudnet dataset is available in the Cloudnet data portal (https://cloudnet.fmi.fi/). The data from the HOLIMO mounted on HoloBalloon will be available on Zenodo (https://zenodo.org/).

References

Becagli, S., and Coauthors, 2019: Biogenic aerosol in the Arctic from eight years of MSA data from Ny Ålesund (Svalbard Islands) and Thule (Greenland). *Atmosphere*, **10**, 349, https://doi.org/10.3390/atmos10070349.

Beck, A., J. Henneberger, S. Schopfer, J. Fugal, and U. Lohmann, 2017: HoloGondel: In situ cloud observations on a cable car in the Swiss Alps using a holographic imager. *Atmos. Meas. Tech.*, **10**, 459–476, https://doi.org/10.5194/amt-10-459-2017.

Beck, L. J., and Coauthors, 2020: Differing mechanisms of new particle formation at two Arctic sites. *Geophys. Res. Lett.*, **48**, e2020GL091334, https://doi.org/10.1029/2020GL091334.

Beine, H. J., S. Argentini, A. Maurizi, G. Mastrantonio, and A. Viola, 2001: The local wind field at Ny-Ålesund and the Zeppelin Mountain at Svalbard. *Meteor. Atmos. Phys.*, **78**, 107–113, https://doi.org/10.1007/s007030170009.

Bennartz, R., and Coauthors, 2013: July 2012 Greenland melt extent enhanced by low-level liquid clouds. *Nature*, **496**, 83–86, https://doi.org/10.1038/nature12002.

Bergeron, T., 1935: On the physics of clouds and precipitation. *Proc. Fifth Assembly of the International Union of Geodesy and Geophysics*, Lisbon, Portugal, International Union of Geodesy and Geophysics, 156–180.

Bigg, E. K., and C. Leck, 2001: Cloud-active particles over the central Arctic Ocean. *J. Geophys. Res.*, **106**, 32 155–32 166, https://doi.org/10.1029/1999JD901152.

Brean, J., M. Dall'Osto, R. Simó, Z. Shi, D. C. S. Beddows, and R. M. Harrison, 2021: Open ocean and coastal new particle formation from sulfuric acid and amines around the Antarctic Peninsula. *Nat. Geosci.*, **14**, 383–388, https://doi.org/10.1038/s41561-021-00751-y.

Burrows, S. M., and Coauthors, 2022: Ice-nucleating particles that impact clouds and climate: Observational and modeling research needs. *Rev. Geophys.*, **60**, e2021RG000745, https://doi.org/10.1029/2021RG000745.

Carlsen, T., and R. O. David, 2022: Spaceborne evidence that ice-nucleating particles influence high-latitude cloud phase. *Geophys. Res. Lett.*, **49**, e2022GL098041, https://doi.org/10.1029/2022GL098041.

Choi, J. H., and Coauthors, 2019: Influence of biogenic organics on the chemical composition of Arctic aerosols. *Global Biogeochem. Cycles*, **33**, 1238–1250, https://doi.org/10.1029/2019GB006226.

Cohen, J., and Coauthors, 2014: Recent Arctic amplification and extreme mid-latitude weather. *Nat. Geosci.*, **7**, 627–637, https://doi.org/10.1038/ngeo2234.

Creamean, J. M., and Coauthors, 2022: Annual cycle observations of aerosols capable of ice formation in central Arctic clouds. *Nat. Commun.*, **13**, 3537, https://doi.org/10.1038/s41467-022-31182-x.

Curry, J. A., J. L. Schramm, W. B. Rossow, and D. Randall, 1996: Overview of Arctic cloud and radiation characteristics. *J. Climate*, **9**, 1731–1764, https://doi.org/10.1175/1520-0442(1996)009<1731:OOACAR>2.0.CO;2.

Dahlke, S., and M. Maturilli, 2017: Contribution of atmospheric advection to the amplified winter warming in the Arctic North Atlantic region. *Adv. Meteor.*, **2017**, 4928620, https://doi.org/10.1155/2017/4928620.

Dall'Osto, M., and Coauthors, 2017: Arctic sea ice melt leads to atmospheric new particle formation. *Sci. Rep.*, **7**, 3318, https://doi.org/10.1038/s41598-017-03328-1.

David, R. O., and Coauthors, 2019: Development of the Droplet Ice Nuclei Counter Zurich (DRINCZ): Validation and application to field-collected snow samples. *Atmos. Meas. Tech.*, **12**, 6865–6888, https://doi.org/10.5194/amt-12-6865-2019.

Dekhtyareva, A., K. Holmén, M. Maturilli, O. Hermansen, and R. Graversen, 2018: Effect of seasonal mesoscale and microscale meteorological conditions in Ny-Ålesund on results of monitoring of long-range transported pollution. *Polar Res.*, **37**, 1508196, https://doi.org/10.1080/17518369.2018.1508196.

Deser, C., J. E. Walsh, and M. S. Timlin, 2000: Arctic sea ice variability in the context of recent atmospheric circulation trends. *J. Climate*, **13**, 617–633, https://doi.org/10.1175/1520-0442(2000)013<0617:ASIVIT>2.0.CO;2.

Dong, X., B. Xi, K. Crosby, C. N. Long, R. S. Stone, and M. D. Shupe, 2010: A 10 year climatology of Arctic cloud fraction and radiative forcing at Barrow, Alaska. *J. Geophys. Res.*, **115**, D17212, https://doi.org/10.1029/2009JD013489.

Doviak, R. J., and D. S. Zrnić, 2006: *Doppler Radar and Weather Observations.* 3rd ed. Dover, 562 pp.

Ebell, K., T. Nomokonova, M. Maturilli, and C. Ritter, 2020: Radiative effect of clouds at Ny-Ålesund, Svalbard, as inferred from ground-based remote sensing observations. *J. Appl. Meteor. Climatol.*, **59**, 3–22, https://doi.org/10.1175/JAMC-D-19-0080.1.

Eleftheriadis, K., S. Vratolis, and S. Nyeki, 2009: Aerosol black carbon in the European Arctic: Measurements at Zeppelin Station, Ny-Ålesund, Svalbard from 1998–2007. *Geophys. Res. Lett.*, **36**, L02809, https://doi.org/10.1029/2008GL035741.

Feltracco, M., and Coauthors, 2020: Interannual variability of sugars in Arctic aerosol: Biomass burning and biogenic inputs. *Sci. Total Environ.*, **706**, 136089, https://doi.org/10.1016/j.scitotenv.2019.136089.

Findeisen, W., 1938: Kolloid-meteorologische Vorgänge bei Niederschlagsbildung. *Meteor. Z.*, **55**, 121–133.

Freud, E., R. Krejci, P. Tunved, R. Leaitch, Q. T. Nguyen, A. Massling, H. Skov, and L. Barrie, 2017: Pan-Arctic aerosol number size distributions: Seasonality and transport patterns. *Atmos. Chem. Phys.*, **17**, 8101–8128, https://doi.org/10.5194/acp-17-8101-2017.

Gierens, R., S. Kneifel, M. D. Shupe, K. Ebell, M. Maturilli, and U. Löhnert, 2020: Low-level mixed-phase clouds in a complex Arctic environment. *Atmos. Chem. Phys.*, **20**, 3459–3481, https://doi.org/10.5194/acp-20-3459-2020.

Goosse, H., and Coauthors, 2018: Quantifying climate feedbacks in polar regions. *Nat. Commun.*, **9**, 1919, https://doi.org/10.1038/s41467-018-04173-0.

Graversen, R. G., and M. Wang, 2009: Polar amplification in a coupled climate model with locked albedo. *Climate Dyn.*, **33**, 629–643, https://doi.org/10.1007/s00382-009-0535-6.

Hall, R. J., E. Hanna, and L. Chen, 2021: Winter Arctic amplification at the synoptic timescale, 1979–2018, its regional variation and response to tropical and extratropical variability. *Climate Dyn.*, **56**, 457–473, https://doi.org/10.1007/s00382-020-05485-y.

Hallett, J., and S. C. Mossop, 1974: Production of secondary ice particles during the riming process. *Nature*, **249**, 26–28, https://doi.org/10.1038/249026a0.

Harrington, J. Y., T. Reisin, W. R. Cotton, and S. M. Kreidenweis, 1999: Cloud resolving simulations of Arctic stratus: Part II: Transition-season clouds. *Atmos. Res.*, **51**, 45–75, https://doi.org/10.1016/S0169-8095(98)00098-2.

Hartmann, M., and Coauthors, 2020: Wintertime airborne measurements of ice nucleating particles in the high Arctic: A hint to a marine, biogenic source for ice nucleating particles. *Geophys. Res. Lett.*, **47**, e2020GL087770, https://doi.org/10.1029/2020GL087770.

Heslin-Rees, D., M. Burgos, H.-C. Hansson, R. Krejci, J. Ström, P. Tunved, and P. Zieger, 2020: From a polar to a marine environment: Has the changing Arctic led to a shift in aerosol light scattering properties? *Atmos. Chem. Phys.*, **20**, 13 671–13 686, https://doi.org/10.5194/acp-20-13671-2020.

Illingworth, A. J., and Coauthors, 2007: Cloudnet: Continuous evaluation of cloud profiles in seven operational models using ground-based observations. *Bull. Amer. Meteor. Soc.*, **88**, 883–898, https://doi.org/10.1175/BAMS-88-6-883.

Kanji, Z. A., L. A. Ladino, H. Wex, Y. Boose, M. Burkert-Kohn, D. J. Cziczo, and M. Krämer, 2017: Overview of ice nucleating particles. *Ice Formation and Evolution in Clouds and Precipitation: Measurement and Modeling Challenges*, *Meteor. Monogr.*, No. 58, Amer. Meteor. Soc., https://doi.org/10.1175/AMSMONOGRAPHS-D-16-0006.1.

Kärcher, B., and C. Marcolli, 2021: Aerosol–cloud interactions: The representation of heterogeneous ice activation in cloud models. *Atmos. Chem. Phys.*, **21**, 15 213–15 220, https://doi.org/10.5194/acp-21-15213-2021.

Karlsson, L., R. Krejci, M. Koike, K. Ebell, and P. Zieger, 2021: A long-term study of cloud residuals from low-level Arctic clouds. *Atmos. Chem. Phys.*, **21**, 8933–8959, https://doi.org/10.5194/acp-21-8933-2021.

Keppas, S. C., J. Crosier, T. W. Choularton, and K. N. Bower, 2017: Ice lollies: An ice particle generated in supercooled conveyor belts. *Geophys. Res. Lett.*, **44**, 5222–5230, https://doi.org/10.1002/2017GL073441.

Kogan, Z. N., D. B. Mechem, and Y. L. Kogan, 2005: Assessment of variability in continental low stratiform clouds based on observations of radar reflectivity. *J. Geophys. Res.*, **110**, D18205, https://doi.org/10.1029/2005JD006158.

Koike, M., and Coauthors, 2019: Year-round in situ measurements of Arctic low-level clouds: Microphysical properties and their relationships with aerosols. *J. Geophys. Res. Atmos.*, **124**, 1798–1822, https://doi.org/10.1029/2018JD029802.

Kondo, Y., L. Sahu, N. Moteki, F. Khan, N. Takegawa, X. Liu, M. Koike, and T. Miyakawa, 2011: Consistency and traceability of black carbon measurements made by laser-induced incandescence, thermal-optical transmittance, and filter-based photo-absorption techniques. *Aerosol Sci. Technol.*, **45**, 295–312, https://doi.org/10.1080/02786826.2010.533215.

Korolev, A., 2007: Limitations of the Wegener–Bergeron–Findeisen mechanism in the evolution of mixed-phase clouds. *J. Atmos. Sci.*, **64**, 3372–3375, https://doi.org/10.1175/JAS4035.1.

——, and G. Isaac, 2003: Phase transformation of mixed-phase clouds. *Quart. J. Roy. Meteor. Soc.*, **129**, 19–38, https://doi.org/10.1256/qj.01.203.

——, and T. Leisner, 2020: Review of experimental studies on secondary ice production. *Atmos. Chem. Phys.*, **20**, 11 767–11 797, https://doi.org/10.5194/acp-20-11767-2020.

——, and Coauthors, 2020: A new look at the environmental conditions favorable to secondary ice production. *Atmos. Chem. Phys.*, **20**, 1391–1429, https://doi.org/10.5194/acp-20-1391-2020.

Lacher, L., U. Lohmann, Y. Boose, A. Zipori, E. Herrmann, N. Bukowiecki, M. Steinbacher, and Z. A. Kanji, 2017: The Horizontal Ice Nucleation Chamber (HINC): INP measurements at conditions relevant for mixed-phase clouds at the High Altitude Research Station Jungfraujoch. *Atmos. Chem. Phys.*, **17**, 15 199–15 224, https://doi.org/10.5194/acp-17-15199-2017.

Ladino, L. A., A. Korolev, I. Heckman, M. Wolde, A. M. Fridlind, and A. S. Ackerman, 2017: On the role of ice-nucleating aerosol in the formation of ice particles in tropical mesoscale convective systems. *Geophys. Res. Lett.*, **44**, 1574–1582, https://doi.org/10.1002/2016GL072455.

Lauber, A., A. Kiselev, T. Pander, P. Handmann, and T. Leisner, 2018: Secondary ice formation during freezing of levitated droplets. *J. Atmos. Sci.*, **75**, 2815–2826, https://doi.org/10.1175/JAS-D-18-0052.1.

Lawrence, Z. D., J. Perlwitz, A. H. Butler, G. L. Manney, P. A. Newman, S. H. Lee, and E. R. Nash, 2020: The remarkably strong Arctic stratospheric polar vortex of winter 2020: Links to record-breaking Arctic Oscillation and ozone loss. *J. Geophys. Res. Atmos.*, **125**, e2020JD033271, https://doi.org/10.1029/2020JD033271.

Lawson, R. P., S. Woods, and H. Morrison, 2015: The microphysics of ice and precipitation development in tropical cumulus clouds. *J. Atmos. Sci.*, **72**, 2429–2445, https://doi.org/10.1175/JAS-D-14-0274.1.

Lee, H., and Coauthors, 2020: Atmospheric new particle formation characteristics in the Arctic as measured at Mount Zeppelin, Svalbard, from 2016 to 2018. *Atmos. Chem. Phys.*, **20**, 13 425–13 441, https://doi.org/10.5194/acp-20-13425-2020.

Lee, S. H., Z. D. Lawrence, A. H. Butler, and A. Y. Karpechko, 2020: Seasonal forecasts of the exceptional Northern Hemisphere winter of 2020. *Geophys. Res. Lett.*, **47**, e2020GL090328, https://doi.org/10.1029/2020GL090328.

Li, G., J. Wieder, J. T. Pasquier, J. Henneberger, and Z. A. Kanji, 2022: Predicting atmospheric background number concentration of ice nucleating particles in the Arctic. *Atmos. Chem. Phys. Discuss.*, https://doi.org/10.5194/acp-2022-21, in press.

Li, H., O. Möhler, T. Petäjä, and D. Moisseev, 2021: Two-year statistics of columnar-ice production in stratiform clouds over Hyytiälä, Finland: Environmental conditions and the relevance to secondary ice production. *Atmos. Chem. Phys.*, **21**, 14 671–14 686, https://doi.org/10.5194/acp-21-14671-2021.

Lloyd, G., and Coauthors, 2015: Observations and comparisons of cloud microphysical properties in spring and summertime Arctic stratocumulus clouds during the ACCACIA campaign. *Atmos. Chem. Phys.*, **15**, 3719–3737, https://doi.org/10.5194/acp-15-3719-2015.

Lohmann, U., F. Lüönd, and F. Mahrt, 2016: Clouds. *An Introduction to Clouds: From the Microscale to Climate*, Cambridge University Press, 1–25, https://doi.org/10.1017/CBO9781139087513.002.

Luke, E. P., F. Yang, P. Kollias, A. M. Vogelmann, and M. Maahn, 2021: New insights into ice multiplication using remote-sensing observations of slightly supercooled mixed-phase clouds in the Arctic. *Proc. Natl. Acad. Sci. USA*, **118**, e2021387118, https://doi.org/10.1073/pnas.2021387118.

Mason, R. H., and Coauthors, 2016: Size-resolved measurements of ice-nucleating particles at six locations in North America and one in Europe. *Atmos. Chem. Phys.*, **16**, 1637–1651, https://doi.org/10.5194/acp-16-1637-2016.

Maturilli, M., 2020: Continuous meteorological observations at station Ny-Ålesund (2011-08 et seq). PANGAEA, accessed 29 October 2022, https://doi.pangaea.de/10.1594/PANGAEA.914979.

——, and K. Kayser, 2017: Arctic warming, moisture increase and circulation changes observed in the Ny-Ålesund homogenized radiosonde record. *Theor. Appl. Climatol.*, **130**, 1434–4483, https://doi.org/10.1007/s00704-016-1864-0.

——, A. Herber, and G. König-Langlo, 2013a: Climatology and time series of surface meteorology in Ny-Ålesund, Svalbard. *Earth Syst. Sci. Data*, **5**, 155–163, https://doi.org/10.5194/essd-5-155-2013.

——, ——, and ——, 2013b: Continuous meteorological observations at station Ny-Ålesund, 1993-08 to 2011-07. PANGAEA, accessed 15 June 2021, https://doi.org/10.1594/PANGAEA.793046.

McFarquhar, G. M., and Coauthors, 2011: Indirect and Semi-Direct Aerosol Campaign. *Bull. Amer. Meteor. Soc.*, **92**, 183–201, https://doi.org/10.1175/2010BAMS2935.1.

Mech, M., M. Maahn, S. Kneifel, D. Ori, E. Orlandi, P. Kollias, V. Schemann, and S. Crewell, 2020: PAMTRA 1.0: the Passive and Active Microwave radiative Transfer tool for simulating radiometer and radar measurements of the cloudy atmosphere. *Geosci. Model Dev.*, **13**, 4229–4251, https://doi.org/10.5194/gmd-13-4229-2020.

Milbrandt, J., and M. Yau, 2005: A multimoment bulk microphysics parameterization. Part II: A proposed three-moment closure and scheme description. *J. Atmos. Sci.*, **62**, 3065–3081, https://doi.org/10.1175/JAS3535.1.

Mioche, G., O. Jourdan, M. Ceccaldi, and J. Delanoë, 2015: Variability of mixed-phase clouds in the Arctic with a focus on the Svalbard region: A study based on spaceborne active remote sensing. *Atmos. Chem. Phys.*, **15**, 2445–2461, https://doi.org/10.5194/acp-15-2445-2015.

Moore, R. H., V. A. Karydis, S. L. Capps, T. L. Lathem, and A. Nenes, 2013: Droplet number uncertainties associated with CCN: An assessment using observations and a global model adjoint. *Atmos. Chem. Phys.*, **13**,4235–4251, https://doi.org/10.5194/acp-13-4235-2013.

Morrison, H., G. de Boer, G. Feingold, J. Harrington, M. D. Shupe, and K. Sulia, 2012: Resilience of persistent Arctic mixed-phase clouds. *Nat. Geosci.*, **5**, 11–17, https://doi.org/10.1038/ngeo1332.

Nielsen, I. E., and Coauthors, 2019: Biogenic and anthropogenic sources of aerosols at the High Arctic site Villum Research Station. *Atmos. Chem. Phys.*, **19**, 10 239–10 256, https://doi.org/10.5194/acp-19-10239-2019.

Nomokonova, T., K. Ebell, U. Löhnert, M. Maturilli, C. Ritter, and E. O'Connor, 2019: Statistics on clouds and their relation to thermodynamic conditions at Ny-Ålesund using ground-based sensor synergy. *Atmos. Chem. Phys.*, **19**, 4105–4126, https://doi.org/10.5194/acp-19-4105-2019.

Norwegian Polar Institute, 2014: Kartdata Svalbard 1:100 000 (s100 Kartdata)/map data. Norwegian Polar Institute, accessed 10 January 2022, https://doi.org/10.21334/npolar.2014.645336c7.

Petzold, A., and M. Schönlinner, 2004: Multi-angle absorption photometry—A new method for the measurement of aerosol light absorption and atmospheric black carbon. *J. Aerosol Sci.*, **35**, 421–441, https://doi.org/10.1016/j.jaerosci.2003.09.005.

Pithan, F., and T. Mauritsen, 2014: Arctic amplification dominated by temperature feedbacks in contemporary climate models. *Nat. Geosci.*, **7**, 181–184, https://doi.org/10.1038/ngeo2071.

Platt, S. M., and Coauthors, 2022: Atmospheric composition in the European Arctic and 30 years of the Zeppelin Observatory, Ny-Ålesund. *Atmos. Chem. Phys.*, **22**, 3321–3369, https://doi.org/10.5194/acp-22-3321-2022.

Quinn, P., G. Shaw, E. Andrews, E. Dutton, T. Ruoho-Airola, and S. Gong, 2007: Arctic haze: Current trends and knowledge gaps. *Tellus*, **59B**, 99–114, https://doi.org/10.1111/j.1600-0889.2006.00236.x.

Ramelli, F., A. Beck, J. Henneberger, and U. Lohmann, 2020: Using a holographic imager on a tethered balloon system for microphysical observations of boundary layer clouds. *Atmos. Meas. Tech.*, **13**, 925–939, https://doi.org/10.5194/amt-13-925-2020.

——, and Coauthors, 2021: Influence of low-level blocking and turbulence on the microphysics of a mixed-phase cloud in an inner-Alpine valley. *Atmos. Chem. Phys.*, **21**, 5151–5172, https://doi.org/10.5194/acp-21-5151-2021.

Rangno, A. L., and P. V. Hobbs, 2001: Ice particles in stratiform clouds in the Arctic and possible mechanisms for the production of high ice concentrations. *J. Geophys. Res.*, **106**, 15 065–15 075, https://doi.org/10.1029/2000JD900286.

Reutter, P., and Coauthors, 2009: Aerosol- and updraft-limited regimes of cloud droplet formation: Influence of particle number, size and hygroscopicity on the activation of cloud condensation nuclei (CCN). *Atmos. Chem. Phys.*, **9**, 7067–7080, https://doi.org/10.5194/acp-9-7067-2009.

Rinaldi, M., and Coauthors, 2017: Atmospheric ice nucleating particle measurements at the high mountain observatory Mt. Cimone (2165 m a.s.l., Italy). *Atmos. Environ.*, **171**, 173–180, https://doi.org/10.1016/j.atmosenv.2017.10.027.

Santachiara, G., L. Di Matteo, F. Prodi, and F. Belosi, 2010: Atmospheric particles acting as ice forming nuclei in different size ranges. *Atmos. Res.*, **96**, 266–272, https://doi.org/10.1016/j.atmosres.2009.08.004.

Schacht, J., and Coauthors, 2019: The importance of the representation of air pollution emissions for the modeled distribution and radiative effects of black carbon in the Arctic. *Atmos. Chem. Phys.*, **19**, 11 159–11 183, https://doi.org/10.5194/acp-19-11159-2019.

Schmale, J., and Coauthors, 2019: Overview of the Antarctic Circumnavigation Expedition: Study of Preindustrial-like Aerosols and Their Climate Effects (ACE-SPACE). *Bull. Amer. Meteor. Soc.*, **100**, 2260–2283, https://doi.org/10.1175/BAMS-D-18-0187.1.

——, P. Zieger, and A. Ekman, 2021: Aerosols in current and future Arctic climate. *Nat. Climate Change*, **11**, 95–105, https://doi.org/10.1038/s41558-020-00969-5.

Schwarz, J. P., and Coauthors, 2006: Single-particle measurements of midlatitude black carbon and light-scattering aerosols from the boundary layer to the lower stratosphere. *J. Geophys. Res.*, **111**, D16207, https://doi.org/10.1029/2006JD007076.

Sedlar, J., M. D. Shupe, and M. Tjernström, 2012: On the relationship between thermodynamic structure and cloud top, and its climate significance in the Arctic. *J. Climate*, **25**, 2374–2393, https://doi.org/10.1175/JCLI-D-11-00186.1.

Shank, L. M., and Coauthors, 2012: Organic matter and non-refractory aerosol over the remote southeast Pacific: Oceanic and combustion sources. *Atmos. Chem. Phys.*, **12**, 557–576, https://doi.org/10.5194/acp-12-557-2012.

Shaw, G. E., 1995: The Arctic haze phenomenon. *Bull. Amer. Meteor. Soc.*, **76**, 2403–2414, https://doi.org/10.1175/1520-0477(1995)076<2403:TAHP>2.0.CO;2.

Shupe, M. D., and J. M. Intrieri, 2004: Cloud radiative forcing of the Arctic surface: The influence of cloud properties, surface albedo, and solar zenith angle. *J. Climate*, **17**, 616–628, https://doi.org/10.1175/1520-0442(2004)017<0616:CRFOTA>2.0.CO;2.

Sinha, P. R., and Coauthors, 2017: Evaluation of ground-based black carbon measurements by filter-based photometers at two Arctic sites. *J. Geophys. Res. Atmos.*, **122**, 3544–3572, https://doi.org/10.1002/2016JD025843.

Skamarock, W. C., and Coauthors, 2019: A description of the Advanced Research WRF Model version 4. NCAR Tech. Note NCAR/TN-556+STR, 145 pp., https://doi.org/10.5065/1dfh-6p97.

Stephens, M., N. Turner, and J. Sandberg, 2003: Particle identification by laser-induced incandescence in a solid-state laser cavity. *Appl. Opt.*, **42**, 3726–3736, https://doi.org/10.1364/ao.42.003726.

Stohl, A., 2006: Characteristics of atmospheric transport into the Arctic troposphere. *J. Geophys. Res.*, **111**, D11306, https://doi.org/10.1029/2005JD006888.

——, and Coauthors, 2007: Arctic smoke—Record high air pollution levels in the European Arctic due to agricultural fires in eastern Europe in spring 2006. *Atmos. Chem. Phys.*, **7**, 511–534, https://doi.org/10.5194/acp-7-511-2007.

Ström, J., and Coauthors, 2003: One year of particle size distribution and aerosol chemical composition measurements at the Zeppelin Station, Svalbard, March 2000–March 2001. *Phys. Chem. Earth*, **28**, 1181–1190, https://doi.org/10.1016/j.pce.2003.08.058.

Sun, Z., and K. P. Shine, 1994: Studies of the radiative properties of ice and mixed-phase clouds. *Quart. J. Roy. Meteor. Soc.*, **120**, 111–137, https://doi.org/10.1002/qj.49712051508.

Susskind, J., G. A. Schmidt, J. N. Lee, and L. Iredell, 2019: Recent global warming as confirmed by AIRS. *Environ. Res. Lett.*, **14**, 044030, https://doi.org/10.1088/1748-9326/aafd4e.

Takahashi, T., Y. Nagao, and Y. Kushiyama, 1995: Possible high ice particle production during graupel–graupel collisions. *J. Atmos. Sci.*, **52**, 4523–4527, https://doi.org/10.1175/1520-0469(1995)052<4523:PHIPPD>2.0.CO;2.

Tjernström, M., and Coauthors, 2014: The Arctic Summer Cloud Ocean Study (ASCOS): Overview and experimental design. *Atmos. Chem. Phys.*, **14**, 2823–2869, https://doi.org/10.5194/acp-14-2823-2014.

Tobo, Y., 2016: An improved approach for measuring immersion freezing in large droplets over a wide temperature range. *Sci. Rep.*, **6**, 32930, https://doi.org/10.1038/srep32930.

——, and Coauthors, 2019: Glacially sourced dust as a potentially significant source of ice nucleating particles. *Nat. Geosci.*, **12**, 253–258, https://doi.org/10.1038/s41561-019-0314-x.

——, J. Uetake, H. Matsui, N. Moteki, Y. Uji, Y. Iwamoto, K. Miura, and R. Misumi, 2020: Seasonal trends of atmospheric ice nucleating particles over Tokyo. *J. Geophys. Res. Atmos.*, **125**, e2020JD033658, https://doi.org/10.1029/2020JD033658.

Tunved, P., J. Ström, and R. Krejci, 2013: Arctic aerosol life cycle: Linking aerosol size distributions observed between 2000 and 2010 with air mass transport and precipitation at Zeppelin Station, Ny-Ålesund, Svalbard. *Atmos. Chem. Phys.*, **13**, 3643–3660, https://doi.org/10.5194/acp-13-3643-2013.

Turetta, C., M. Feltracco, E. Barbaro, A. Spolaor, C. Barbante, and A. Gambaro, 2021: A year-round measurement of water-soluble trace and rare earth elements in Arctic aerosol: Possible inorganic tracers of specific events. *Atmosphere*, **12**, 694, https://doi.org/10.3390/atmos12060694.

Verheggen, B., and Coauthors, 2007: Aerosol partitioning between the interstitial and the condensed phase in mixed-phase clouds. *J. Geophys. Res.*, **112**, D23202, https://doi.org/10.1029/2007JD008714.

Wegener, A., 1911: *Thermodynamik der Atmosphäre.* J. A. Barth, 331 pp.

Weinbruch, S., D. Wiesemann, M. Ebert, K. Schütze, R. Kallenborn, and J. Ström, 2012: Chemical composition and sources of aerosol particles at Zeppelin Mountain (Ny Ålesund, Svalbard): An electron microscopy study. *Atmos. Environ.*, **49**, 142–150, https://doi.org/10.1016/j.atmosenv.2011.12.008.

Wendisch, M., and Coauthors, 2017: Understanding causes and effects of rapid warming in the Arctic. *Eos*, **98**, 22–26, https://doi.org/10.1029/2017EO064803.

——, and Coauthors, 2019: The Arctic cloud puzzle: Using ACLOUD/PASCAL multiplatform observations to unravel the role of clouds and aerosol particles in Arctic amplification. *Bull. Amer. Meteor. Soc.*, **100**, 841–871, https://doi.org/10.1175/BAMS-D-18-0072.1.

Wieder, J., and Coauthors, 2022a: Retrieving ice nucleating particle concentration and ice multiplication factors using active remote sensing validated by in situ observations. *Atmos. Chem. Phys.*, **22**, 9767–9797, https://doi.org/10.5194/acp-22-9767-2022.

——, and Coauthors, 2022b: Unveiling atmospheric transport and mixing mechanisms of ice-nucleating particles over the Alps. *Atmos. Chem. Phys.*, **22**, 3111–3130, https://doi.org/10.5194/acp-22-3111-2022.

Willis, M. D., W. R. Leaitch, and J. P. Abbatt, 2018: Processes controlling the composition and abundance of Arctic aerosol. *Rev. Geophys.*, **56**, 621–671, https://doi.org/10.1029/2018RG000602.

Young, G., and Coauthors, 2016: Observed microphysical changes in Arctic mixed-phase clouds when transitioning from sea ice to open ocean. *Atmos. Chem. Phys.*, **16**, 13 945–13 967, https://doi.org/10.5194/acp-16-13945-2016.

Zangrando, R., E. Barbaro, P. Zennaro, S. Rossi, N. M. Kehrwald, J. Gabrieli, C. Barbante, and A. Gambaro, 2013: Molecular markers of biomass burning in Arctic aerosols. *Environ. Sci. Technol.*, **47**, 8565–8574, https://doi.org/10.1021/es400125r.

Zuidema, P., and Coauthors, 2005: An Arctic springtime mixed-phase cloudy boundary layer observed during SHEBA. *J. Atmos. Sci.*, **62**, 160–176, https://doi.org/10.1175/JAS-3368.1.